Applications in Engineering Science 17 (2024) 100174

Contents lists available at ScienceDirect

Applications in Engineering Science

journal homepage: www.elsevier.com/locate/apples

Mechanical response of tensegrity-origami solar modules

Fernando Fraternali [a,*], Julia de Castro Motta [a], Giovanni Germano [a], Enrico Babilio [b], Ada Amendola [a]

[a] Department of Civil Engineering, University of Salerno, Fisciano (SA), 84084, Italy
[b] Department of Structures for Engineering and Architecture (DiSt), University of Naples "Federico II", Naples, 80134, Italy

ARTICLE INFO

Keywords:
Origami systems
Tensegrity structures
Solar modules
Force–displacement response

ABSTRACT

This work studies the mechanics of novel origami solar modules with tensegrity architecture for integration in the dynamic solar façades of energy-efficient buildings. The analyzed modules are deployed by adjusting the rest lengths of cables attached to given nodes, so as to form a tensegrity origami. Their stiffness is tuned by adjusting the pretension of the actuation cables, when the deployment motion is locked. The insertion of solar thermal or photovoltaic panels into the rigid elements of the module makes it possible to form positive-energy solar systems. The work studies the kinematics and the mechanics of the investigated structures through analytic and numerical methods. Two folding motions are examined: to open and close the modules and to track sun rays. The rapid prototyping of a physical mock-up permits an experimental validation of the force–displacement response in a given configuration of the sun-tracking motion. A procedure for the computation of the fundamental vibration modes and vibration frequencies of a quadrangular solar module is also given, and the expected response of the system under wind loading is outlined.

1. Introduction

The energy efficiency of 'green' buildings can be achieved by both minimizing heat and air conditioning consumption and by using energy harvesting techniques from renewable sources (solar, wind, and geothermal) (Çiner and Dogan-Saglamtimur, 2019; Chen et al., 2022; Ala-Juusela et al., 2021; Awadh, 2017). The building's envelope plays a fundamental role in determining its response to periodic and exceptional modifications to the surrounding environment. Since most buildings are taller than they are wide, architects and engineers pay special attention to the design of vertical façades that combine eye-catching shapes with energy harvesting capabilities and environmental benefits (Attoye et al., 2017; Li and Cui, 2021; Bakhshoodeh et al., 2022; Mir, 2011). Solar façades often form the envelope to environment-responsive buildings (Attoye et al., 2017; Li and Cui, 2021). A photovoltaic (PV) solar façade or shading device uses conventional PV cells and/or thin-film solar materials to form architectural modules of various textures, translucency, and colors (refer, e.g., to façades composed of dye-sensitized solar cells) that transform solar irradiation into electricity (Attoye et al., 2017). Rooftop PV systems and solar-thermal modules (Li and Cui, 2021) are also employed. The wide category of Building Integrated Photovoltaics (BIPV) (Attoye et al., 2017; Vassiliades et al., 2022) encompasses several solutions for integrating PV cells into the envelope of energy efficient buildings (nearly zero or positive-energy buildings, see Ala-Juusela et al. (2021) for definitions and concepts).

Origami systems are deployable thin-walled structures that can change their shape by folding and unfolding. Due to their highly adaptive character, such systems have been extensively investigated recently for a variety of uses (see, e.g., the comprehensive review presented in Fonseca et al. (2022), and the references). Their methods of forming deployable membranes (Miura, 1985; Seffen, 2012), multistable structures (Li and Pellegrino, 2020; Lu et al., 2023a), systems with high packing capacity (Lu et al., 2023b) and mechanical metamaterials combined with on-demand deployability and collapsibility merit attention (Schenk and Guest, 2013; Zhai et al., 2018; Pratapa et al., 2018). Origami-inspired systems find applications in robotics, foldable architecture, medicine, and engineering (Fonseca et al., 2022; Miura, 1985; Salazar et al., 2017; Liu et al., 2023). The dynamic curtain walls that form the piston-activated and umbrella-shaped sunscreens of the Al Bahar towers in Abu Dhabi are well-known examples of origami-inspired designs of building façades (Armstrong et al., 2013; Karanouh and Kerber, 2015). Each screen is a triangulated origami structure that can fold perpendicularly to the building façades (the shading wall is two meters from the building façade). Building façades based on kaleidocycle origami rings have been proposed and optimized to enhance the natural lighting in the interior of a building (Elghazi

* Corresponding author.
E-mail address: f.fraternali@unisa.it (F. Fraternali).

https://doi.org/10.1016/j.apples.2023.100174
Received 3 December 2023; Accepted 12 December 2023
Available online 19 December 2023

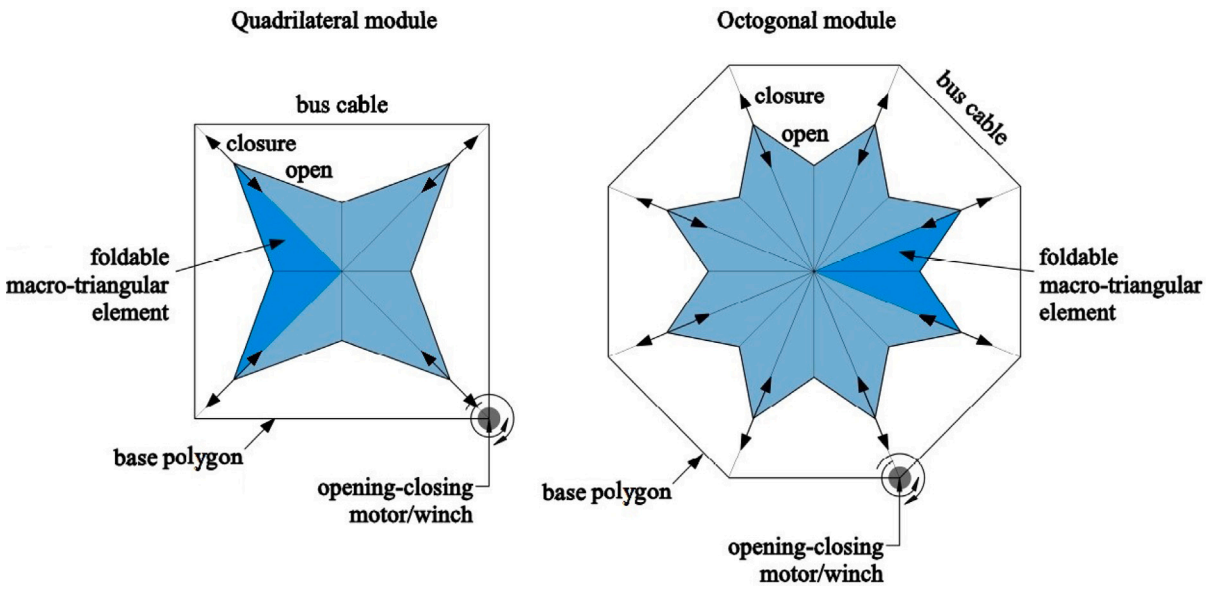

Fig. 1. Frontal views of quadrilateral and octagonal versions of the solar eye module, with illustration of the primary folding motion.

et al., 2014; Wagdy et al., 2015). Pesenti et al. (2015) analyzed several different origami patterns, comparing their potential for applications on adaptive façades with shape memory alloy (SMA) activation. Andreozzi et al. (2016) conducted a study on the level of lighting indoors due to different degrees of deployment of an adaptive origami façade. Chen et al. (2019) have investigated the use of shape memory polymers to form origami sheets endowed with deployable solar panels. Recently, lightweight and low-energy consumption tensegrity redesigns of the origami façades of the Al Bahar towers, employing stretching and contraction of elastic cables by electro-mechanical actuators to activate the opening–closing mechanism of origami sunscreens have been formulated (Fraternali et al., 2015b; Babilio et al., 2019; Miranda et al., 2020). Tensegrity structures have found exciting applications to form deployable systems, such as, for example, robots (Karnan et al., 2017), bridges and mats (Tibert and Pellegrino, 2003). As general references, one can see the admirable textbooks by De Oliveira and Skelton (2009) and Miura and Pellegrino (2020).

This work studies the mechanics of novel origami modules using tensegrity architecture, shaped like 'solar eyes'. Such systems can be employed to tessellate curtain walls, glazing panels, windows, sunscreens, rooftops, and/or active building skins that show enhanced solar energy harvesting capacity. The analyzed solar eyes are equipped with PV or solar-thermal (T) panels that permit the production of electrical energy or air/water heating for the building. The solar eye module may have a generic polygonal shape and can exhibit two different folding motions or deformation histories. A primary folding motion of the solar module is similar to that analyzed in Fraternali et al. (2015b), Babilio et al. (2019), Miranda et al. (2020), but it is activated by a completely different cable mechanism, which has led us to produce an unprecedented concept: a tensegrity origami with arbitrary polygonal shape. A secondary folding motion is superimposed on the primary motion to endow the module with sun-tracking capacity and to optimize the diffusion of natural light into the interior of the building. Such a motion was not included in the solar modules with fixed polygonal geometry studied in Fraternali et al. (2015b), Babilio et al. (2019), Miranda et al. (2020). Both folding motions are activated by changing the rest lengths of the cables forming the module. These lengths can be controlled either manually (by cranks) or through low-consumption electric motor winches. The module entails considerable economic advantages compared to the modules with electro-mechanical actuators presented in Miranda et al. (2020), making the BIPV systems analyzed in this work particularly attractive from an energy point of view and potentially of positive energy type (Ala-Juusela et al., 2021). The structure of the paper is as follows. We begin by presenting the conceptual design of a solar eye with an arbitrary polygonal geometry (Section 2). Next, we illustrate the special case of a quadrilateral module in Section 3 by describing the unit cell structure, the primary and secondary folding motions, and the rapid prototyping techniques employed to fabricate a physical mock-up (see also Supplementary Materials). Sections 4 and 5 illustrate the kinematics of the folding motions of the solar eye, while Section 6 studies the stiffness properties of the system when the folding motions are locked. We end in Section 7 by describing a procedure for the computation of the fundamental vibration modes and vibration frequencies of a quadrangular solar eye. This procedure leads us to identify the possible types of response of the system under wind loading. Finally, concluding remarks and directions for future work are presented in Section 8.

2. Design principles of tensegrity-origami modules

The solar modules analyzed in this work exhibit a projection with a generic polygonal shape on the plane parallel to the building façade. We denote such a projection, in correspondence to the unfolded ('closed') configuration of the system, with the name 'base polygon', and let p denote the number of sides of this polygon. As shown in Fig. 1, the solar module is formed by the collection of p, foldable 'macro-triangles,' which are delimited by the segments joining the vertices of the base polygon with its center. In turn, each macro-triangle is composed of two elementary 'micro-triangles' housing PV or T panels, which fold out of the plane when opening and closing the screen ('sunscreen panels'). The activation cables governing this ('primary') folding motion connect the vertices of the folded macro-triangles to the center (opening cables) and to the corners (closing cables) of the base polygon. These cables are joined to a 'bus cable' running along the perimeter of the base polygon, so that the opening and closing mechanisms of the different micro-triangles can be operated simultaneously (refer to Section 3 for more details). Solar façades that tessellate origami modules with different geometries are shown in Fig. 2.

The folding motion/deformation process of the solar module is obtained by simply adjusting the rest lengths of the cables without stretching them, as opposed to the module studied in Miranda et al. (2020) that is folded by elastically deforming the perimeter cables.

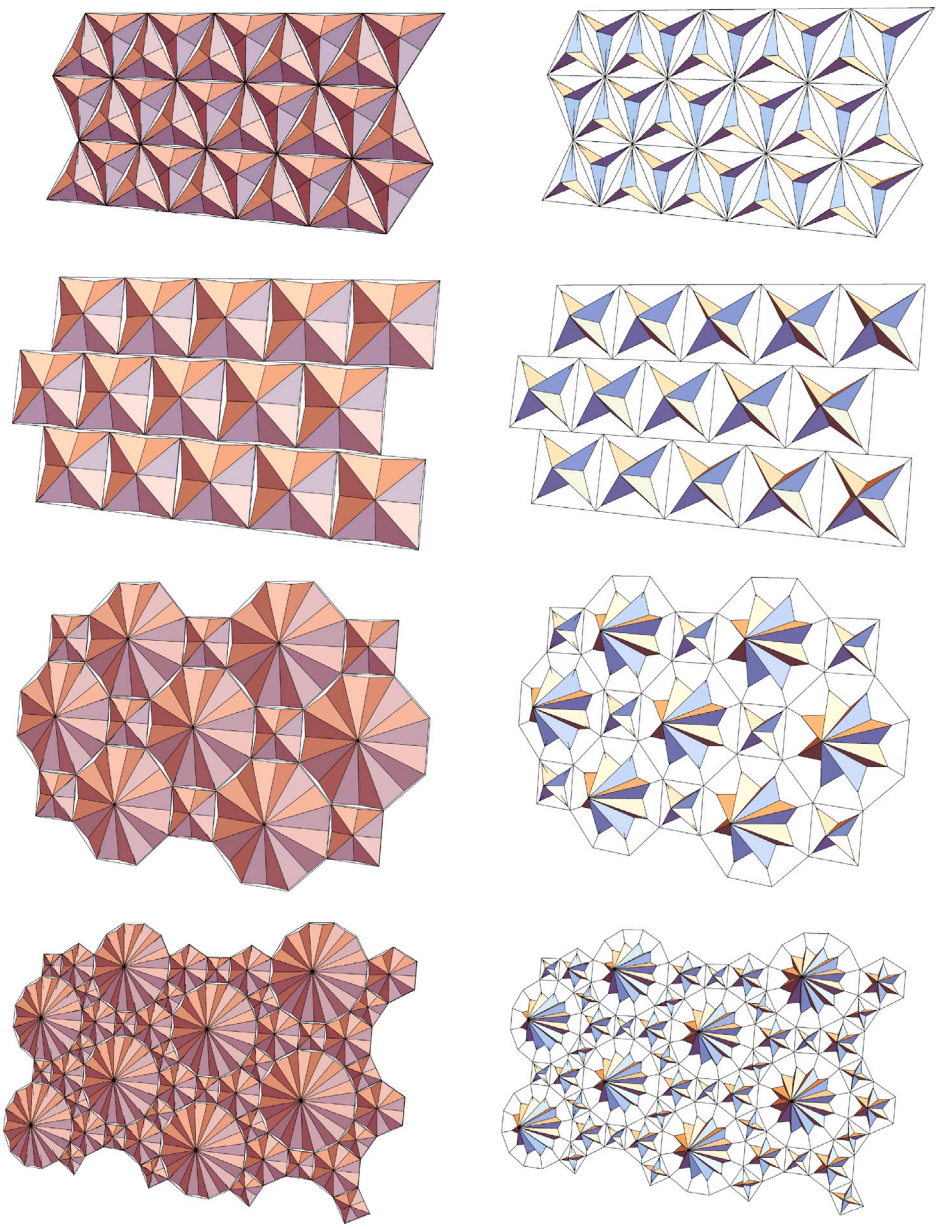

Fig. 2. Partially closed (left) and partially open (right) configurations of origami solar facades with different textures. The textures of the two top panels are composed of modules with identical shapes. Those of the two bottom panels are instead formed by composite assemblies of modules with different polygonal shapes.

The change of the rest length can be obtained by using low energy-consumption electric winches or motors or manually through crank winches (Fig. 1). When the rest length of the 'primary motion activation cables' is kept fixed by locking the activation winches/motors, the system is in a stable configuration, since the perturbation of this configuration is contrasted by the elastic and prestress-induced (or 'geometric') stiffness of the cables (Fraternali et al., 2015b). On the other hand, when the change of the rest lengths of the cables is permitted by unlocking the activation winches/motors, the unit exhibits a rigid-body folding (or 'opening') motion out of plane (cf. Fig. 1).

The sun-tracking ability of the module is made possible by introducing a secondary folding motion of the micro-triangles plates, which allows these elements to rotate about the 'diagonal' edges (or 'legs') connecting the perimeter vertices with the center of the unit (see Fig. 3). The variation of the dihedral angle θ comprised between the plane of the supporting frame of the generic micro-triangle ('base plane') and the plane of the rotated micro-triangle plate ('folded plane') is guided by two bars forming a scissor-type tensegrity structure connecting these planes (the term 'scissor' refers to the configuration of the structure in the almost closed configuration, see Fig. 3). Each bar has one extremity connected to a ball joint attached to the folded plane, which is placed at a distance c from the diagonal edge of the micro-triangle (Fig. 3). The other extremity of the bar is attached to a guiding cable lying on the base plane. One of the two bars of the scissor structure is attached to an opening cable at its bottom extremity (the red cable in Fig. 3), while the other bar is connected to a closing cable (the brown cable in Fig. 3). These two cables are joined to a looped bus cable (the green cable in Fig. 3), in such a way that the opening and closing motion of the micro-triangle can be actuated through a unique controller.

Hereafter, we refer to the cables shown in Fig. 3 as 'secondary motion activation cables'. It is worth noting that the two bars of the scissor tensegrity point to different edges of the folded micro-triangle, which are opposite the diagonal edge. Such bars exhibit symmetrical motions with respect to the central axis of the structure when the micro-triangle is folded, being placed parallel to the supporting frame in the unfolded (or closed) configuration and orthogonal to such a frame in

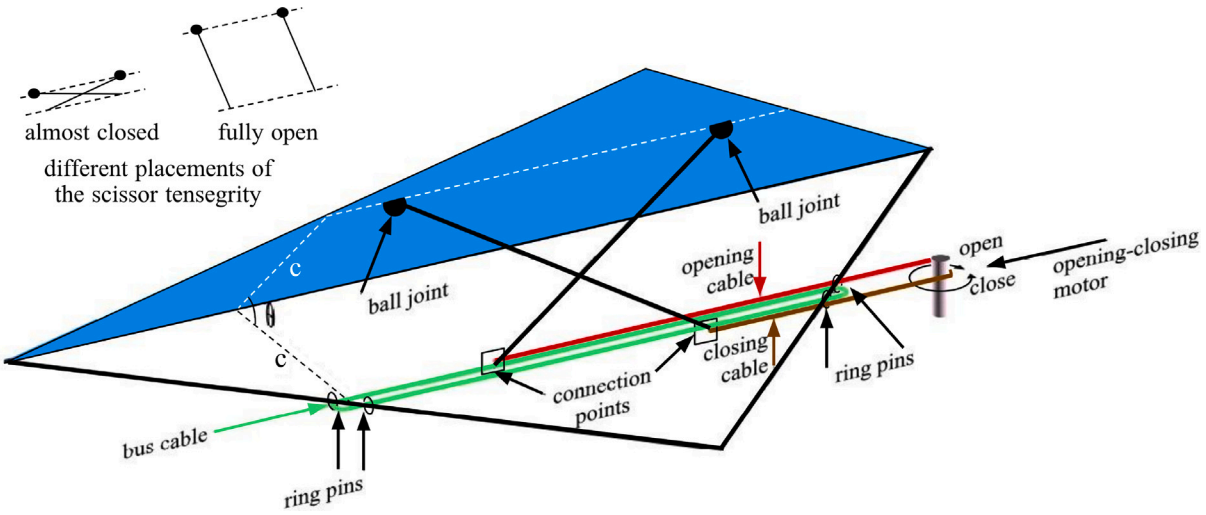

Fig. 3. Illustration of the secondary folding motion of a micro-triangle.

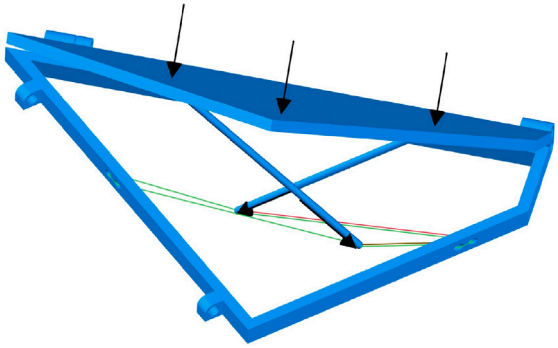

Fig. 4. Deformation of the base cable of the scissor tensegrity under the action of external forces.

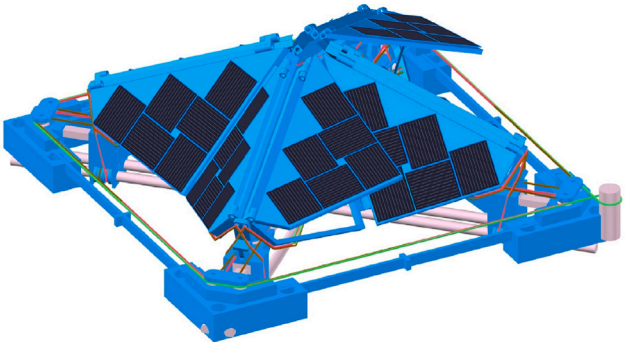

Fig. 5. Illustrative isometric view of the quadrilateral module.

the fully folded (or open) configuration (see Fig. 3). The secondary folding motion is controlled by changing the rest lengths of the base cables of the scissor tensegrity upon again using energy-consumption electric winches or motors or crank winches, as in the case of the primary motion. When the actuation winch/motor is locked and a suitable pre-tension is applied to the base cables, the secondary folding motion is stabilized by forcing the rest length of such members to be fixed, so that any perturbations of the folded configuration are contrasted by the material and geometric stiffness of the cables (Fraternali et al., 2015b). Under the action of external forces (e.g., wind forces), the bars forming the scissor tensegrities will bend the secondary cables of the stabilized system to create a tensegrity equilibrium configuration (see Fig. 4 and Section 6.2).

3. The special case of a quadrilateral module

Let us now focus on the special case of a quadrilateral solar eye module, which is composed of four macro-triangles and eight micro-triangles, with the latter hosting PV and/or T panels (the black elements in the illustrative Fig. 5). The solutions and techniques presented with reference to this module can be easily generalized to modules with different polygonal geometries.

The opening and closing cables governing the primary folding motion of the quadrilateral module (i.e., the primary activation cables) run through guiding pulleys that are placed in the four corners of the base perimeter, in the center of the module, and in correspondence to the sliding blocks along the diagonal edges (Fig. 6). Each sliding block runs along a diagonal track and is connected to an opening and a closing cable that activate the primary folding motion of two micro-triangles, placed on opposite sides with respect to a diagonal segment. Overall, we have a total of four sets of opening and closing cables that activate the primary folding motion. All such activation cables are joined to a unique bus cable running along the base perimeter, which is in turn connected to a winch/motor, so that the primary folding motion can be activated simultaneously in correspondence to all the macro-triangles of the unit. The activation of the secondary folding motion is as described in the previous section.

A demonstrative mock-up of a quadrilateral module was assembled in the Rapid Prototyping Laboratory (RPL) of the University of Salerno using ordinary 3D printers, metallic parts, DC motors, and motor controllers (Fig. 7). The mock-up is contained in square with a 290.22-mm edge and is composed of eight right micro-triangles with a hypotenuse of 183 mm and maximum height above the base supporting frame of 89.2 mm. The reader is referred to Supplementary Materials for a detailed description of the operation of the physical mock-up.

4. Kinematics of the primary folding motion

Let $\mathcal{F}$ denote the generic macro-triangle composing the unit cell of a solar module with generic polygonal shape, which we suppose to be isosceles with apex angle $0 < \alpha < \pi$ (Fig. 8). The analogous module of the systems studied in Miranda et al. (2020) shows a fixed value of such an angle, which is equal to $2\pi/3$. We take the unfolded (flat) configuration of such an element as reference, and we introduce a Cartesian frame with origin at node 0 in Fig. 8 and unit vectors

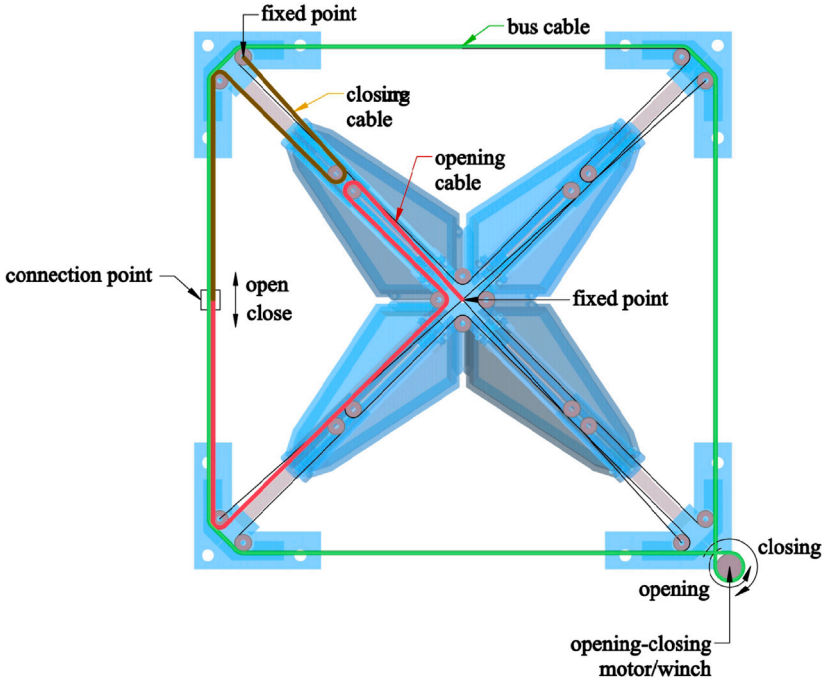

Fig. 6. Opening–closing mechanism of the primary folding motion of a quadrilateral module obtained by changing the rest length of the activation cables.

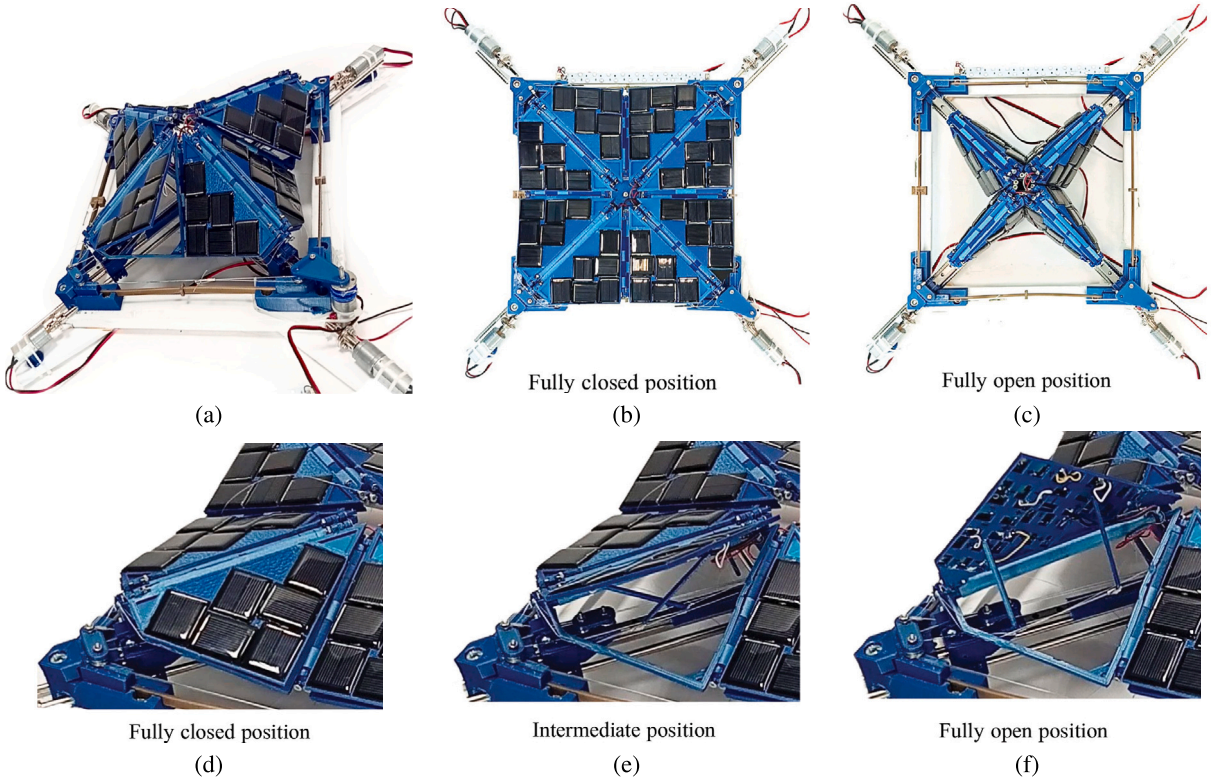

Fig. 7. (a) 3D view of the fabricated mock-up of a quadrilateral module. (b–f) Frames extracted from videos of the opening and closing mechanisms of the primary (b–c) and the secondary (d–f) folding motions (see Movies S1–S3 of Supplementary Materials).

$\{\mathbf{e}_1, \mathbf{e}_2, \mathbf{e}_3\}$, such that $\mathbf{e}_1$ is aligned with a diagonal edge (or leg) of $\mathcal{F}$; $\mathbf{e}_2$ is orthogonal to $\mathbf{e}_1$ and lies in the plane of the unfolded configuration; and $\mathbf{e}_3$ is orthogonal to such a plane (Fig. 8).

We study the primary folding deformation (or quasi-static motion) of $\mathcal{T}$ under the following *displacement constraints*: node 0 is constrained to move along the positive $\mathbf{e}_3$ axis; node 1 is constrained to move along the 0–1 segment of the unfolded configuration; node 2 is constrained to move in the plane formed by $\mathbf{e}_3$ and the bisector of the angle α encompassed by the macro-triangle in the unfolded configuration, with negative displacement component along the $\mathbf{e}_3$ axis; and the displacement vector of node 3 is obtained by rotating that of node 1 by the angle α about $\mathbf{e}_3$. In addition, we restrict our attention to a rigid

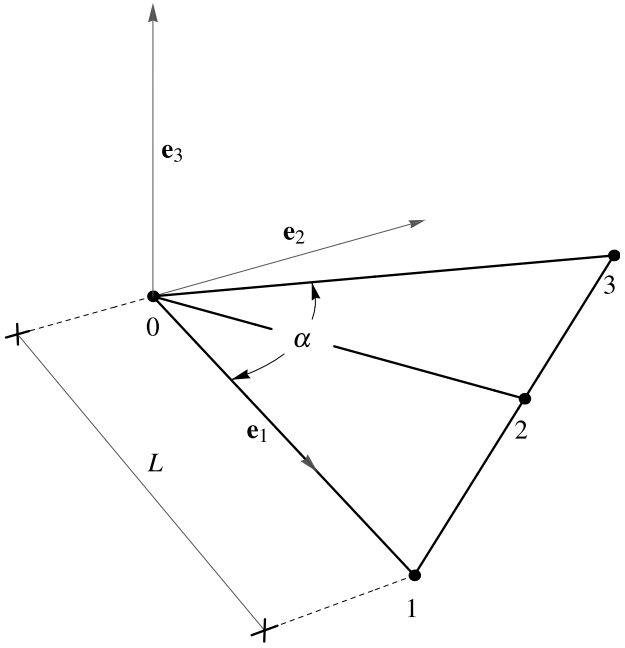

Fig. 8. Reference configuration of the generic macro triangle $\mathcal{T}$..

origami motion by complementing the above displacement constraints with the following *rigidity constraints*:

$$L_{0i} = \ell_{0i}\,, \quad i = 1,2,3 \tag{1}$$

$$L_{2j} = \ell_{2j}\,, \quad j = 1 \text{ or } j = 3 \tag{2}$$

L_{ij} and ℓ_{ij} being the Euclidean distances between two nodes i and j in the reference configuration and the folded configuration, respectively. Such quantities are computed as follows:

$$L_{ij} = \sqrt{(\mathbf{X}_i - \mathbf{X}_j)\cdot(\mathbf{X}_i - \mathbf{X}_j)}\,, \tag{3}$$

$$\ell_{ij} = \sqrt{(\mathbf{x}_i - \mathbf{x}_j)\cdot(\mathbf{x}_i - \mathbf{x}_j)}\,, \tag{4}$$

where $\mathbf{X}_i$ and $\mathbf{x}_i$ are the position vectors of the generic node $i \in \{0,1,2,3\}$ in correspondence to the reference configuration and the folded configuration, respectively. It is easily recognized that it results in $L_{01} = L_{03} = L$, $L_{21} = L_{23} = L\sin\alpha/2$, and $L_{02} = L\cos\alpha/2$ (Fig. 8).

Let now $\mathbf{R}_\alpha = \mathbf{R}(\alpha)$ denote the rotation tensor defined as follows:

$$\begin{aligned}\mathbf{R}(\alpha) :=& \cos\alpha\,(\mathbf{e}_1\otimes\mathbf{e}_1 + \mathbf{e}_2\otimes\mathbf{e}_2)\\ &+ \sin\alpha\,(\mathbf{e}_2\otimes\mathbf{e}_1 - \mathbf{e}_1\otimes\mathbf{e}_2) + \mathbf{e}_3\otimes\mathbf{e}_3\,,\end{aligned} \tag{5}$$

which rotates the vectors lying in the $\mathbf{e}_1 - \mathbf{e}_2$ plane of an angle α counterclockwise. It is easily observed that it results in (Fig. 8)

$$\mathbf{X}_0 = \mathbf{0}\,, \tag{6}$$

$$\mathbf{X}_1 = L\mathbf{e}_1\,, \tag{7}$$

$$\mathbf{X}_2 = L\cos\frac{\alpha}{2}\left(\cos\frac{\alpha}{2}\mathbf{e}_1 + \sin\frac{\alpha}{2}\mathbf{e}_2\right), \tag{8}$$

$$\mathbf{X}_3 = \mathbf{R}_\alpha\mathbf{X}_1\,, \tag{9}$$

and that the assumed displacement constraints allow us to write

$$\mathbf{x}_0 = \mathbf{X}_0 + a_0 L\mathbf{e}_3\,, \tag{10}$$

$$\mathbf{x}_1 = \mathbf{X}_1 - a_1 L\mathbf{e}_1\,, \tag{11}$$

$$\mathbf{x}_2 = \mathbf{X}_2 - a_2 L\left(\cos\frac{\alpha}{2}\mathbf{e}_1 + \sin\frac{\alpha}{2}\mathbf{e}_2\right) - a_3 L\mathbf{e}_3\,, \tag{12}$$

$$\mathbf{x}_3 = \mathbf{R}_\alpha\mathbf{x}_1\,, \tag{13}$$

where

$$a_0 \geq 0\,, \quad 0 \leq a_1 \leq 1\,, \quad 0 \leq a_2 \leq \cos\frac{\alpha}{2}\,, \quad a_3 \geq 0\,. \tag{14}$$

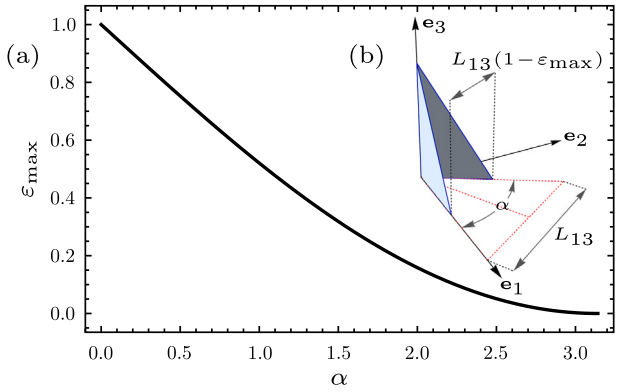

Fig. 9. (a) Plot of ε_{max} vs. α. (b) Illustration of the fully folded configuration.

The dimensionless scalar parameters a_i ($i = \{0,\ldots,3\}$), which appear in Eqs. (10)–(14), are to be determined using the rigidity constraints. For further use, we set

$$L_{13}(1-\varepsilon) = \ell_{13}\,, \tag{15}$$

where ε is a non-negative scalar parameter that describes either the change of the rest length of the closure cable 1–3 of $\mathcal{T}$ (deployment phase) or the opposite of the engineering strain characterizing the stretching of such a cable (stabilization phase). Upon taking squares of both sides of Eqs. (1)–(2) and moving all terms to the left side, it is easy to show that the rigidity constraints can be reduced to the following system of nonlinear algebraic equations

$$a_0^2 + a_1\,(a_1 - 2) = 0\,, \tag{16}$$

$$(a_0 + a_3)^2 + a_2\left(a_2 - 2\cos\frac{\alpha}{2}\right) = 0\,, \tag{17}$$

$$a_1^2 + a_2^2 + a_3^2 + a_1\left(\cos\alpha - 2a_2\cos\frac{\alpha}{2} - 1\right) = 0\,. \tag{18}$$

We add the following equation

$$\varepsilon^2 + 2\,(a_1 - \varepsilon) \;-\; a_1^2 = 0\,, \tag{19}$$

to Eqs. (16)–(18), which follows from taking squares of both sides of Eq. (15) and moving all terms to the left side. The Eqs. (16)–(19) admit eight sets of solutions for the scalar parameters a_i, but only one of such set of solutions matches the constraints (14), namely

$$a_0 = \sqrt{\varepsilon\,(2-\varepsilon)}\,, \tag{20}$$

$$a_1 = \varepsilon\,, \tag{21}$$

$$a_2 = \frac{\varepsilon}{2}\,\frac{\sin\alpha + 2\cos\frac{\alpha}{2}}{1-(1-\varepsilon)\sin\frac{\alpha}{2}}\,, \tag{22}$$

$$a_3 = \sqrt{\varepsilon\,(2-\varepsilon)}\;\sin\frac{\alpha}{2}\,\frac{1-\varepsilon-\sin\frac{\alpha}{2}}{1-(1-\varepsilon)\sin\frac{\alpha}{2}}\,. \tag{23}$$

The maximum value of ε, which we denote ε_{max}, corresponds to the fully folded configuration of $\mathcal{T}$. Let $a_{2,max}$ denote the value of a_2 obtained by setting $\varepsilon = \varepsilon_{max}$ into Eq. (22). Using the third constraint (14), we easily obtain

$$a_{2,max} = \cos\frac{\alpha}{2}\,, \tag{24}$$

which implies, from Eq. (22)

$$\varepsilon_{max} = 1 - \sin\frac{\alpha}{2}\,. \tag{25}$$

Fig. 9 shows the plot of the ε_{max} vs. α law given by Eqs. (25), while Fig. 10 shows plots of the solutions (20)–(23), with the a_2 vs. ε and the a_3 vs. ε laws determined for selected values of α. It is worth computing the limiting values of a_1, a_2 and ε_{max} for $\alpha \to 0$ and $\alpha \to \pi$. Using

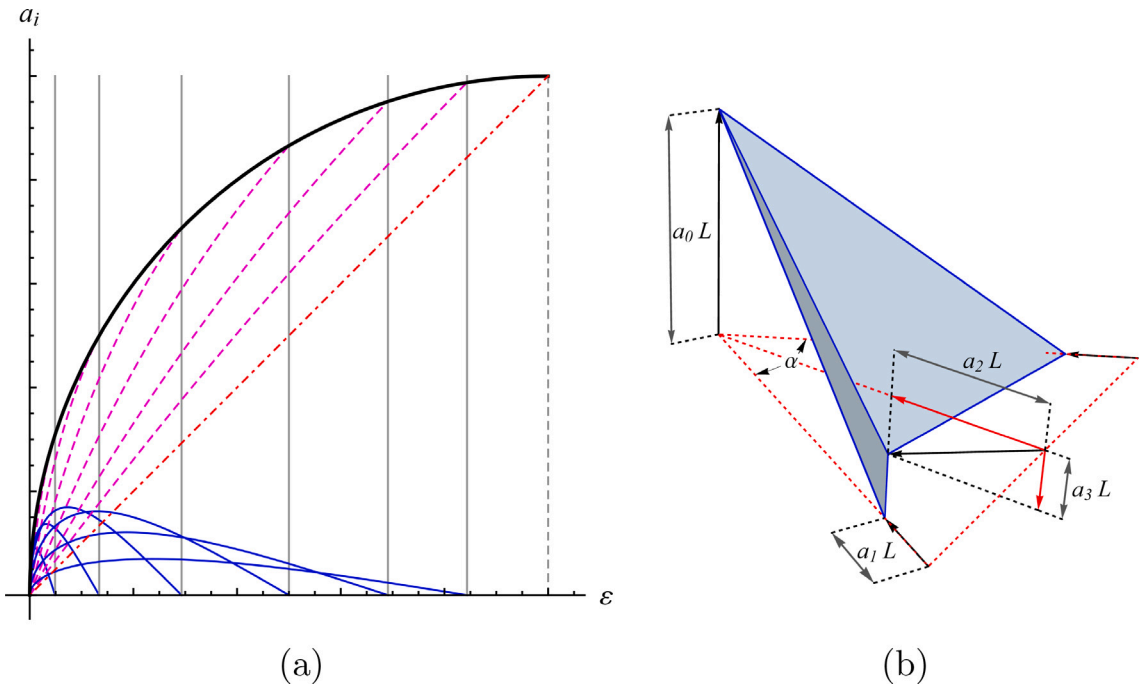

Fig. 10. (a) Plots of the displacement parameters a_i vs. ε, as given by Eqs. (20)–(23). The solid black curve plots a_0 vs. ε; the dash–dotted red line gives a_1 as a function of ε; the dashed magenta curves and the solid blue curves respectively plot the a_2 vs. ε and the a_3 vs. ε laws, which correspond to the following values of α, from left to right: $4\pi/5$, $2\pi/3$, $\pi/2$, $\pi/3$, $\pi/5$, $\pi/10$. (b) Illustration of the geometric meaning of the a_i parameters.

Eqs. (20)–(23) and (25), it is easily shown that it results in $a_2 \to a_1$, $a_3 \to 0$, and $\varepsilon_{\max} \to 1$, for $\alpha \to 0$. On the other hand, for $\alpha \to \pi$, we obtain $a_2 \to 0$, $a_3 \to -a_0$, and $\varepsilon_{\max} \to 0$.

We conclude this section by observing that we can give a compact expression to the primary folding deformation of a micro-triangle forming $\mathcal{T}$. Let us examine, e.g., the folding deformation of the $\overset{\triangle}{012}$ micro-triangle by introducing the following 3×3 matrices

$$\begin{aligned} \hat{\mathbf{X}} &= \left\{ \ \hat{\mathbf{X}}_1 - \hat{\mathbf{X}}_0 \ \middle| \ \hat{\mathbf{X}}_2 - \hat{\mathbf{X}}_0 \ \middle| \ \hat{\mathbf{X}}_4 - \hat{\mathbf{X}}_0 \ \right\}, \\ \hat{\mathbf{x}} &= \left\{ \ \hat{\mathbf{x}}_1 - \hat{\mathbf{x}}_0 \ \middle| \ \hat{\mathbf{x}}_2 - \hat{\mathbf{x}}_0 \ \middle| \ \hat{\mathbf{x}}_4 - \hat{\mathbf{x}}_0 \ \right\}, \end{aligned} \tag{26}$$

where $\hat{\mathbf{X}}_i$ and $\hat{\mathbf{x}}_i$ denote the column vectors collecting the Cartesian components of the vectors $\mathbf{X}_i$ and $\mathbf{x}_i$ ($i = 0, \dots, 4$), respectively, and we have set

$$\mathbf{X}_4 = \mathbf{X}_0 + \frac{(\mathbf{X}_1 - \mathbf{X}_0) \times (\mathbf{X}_2 - \mathbf{X}_0)}{S}, \tag{27}$$

$$\mathbf{x}_4 = \mathbf{x}_0 + \frac{(\mathbf{x}_1 - \mathbf{x}_0) \times (\mathbf{x}_2 - \mathbf{x}_0)}{s}, \tag{28}$$

with

$$S = \|(\mathbf{X}_1 - \mathbf{X}_0) \times (\mathbf{X}_2 - \mathbf{X}_0)\| \tag{29}$$

and

$$s = \|(\mathbf{x}_1 - \mathbf{x}_0) \times (\mathbf{x}_2 - \mathbf{x}_0)\|. \tag{30}$$

Here, $\times$ denotes the symbol of cross product between vectors. It is easily shown that we can write

$$\hat{\mathbf{x}}_i = \hat{\mathbf{x}}_0 + \hat{\mathbf{R}}'(\hat{\mathbf{X}}_i - \hat{\mathbf{X}}_0), \qquad (i = 1, 2) \tag{31}$$

$\hat{\mathbf{R}}'$ being the rotation matrix defined as (Sumner and Popovic, 2004)

$$\hat{\mathbf{R}}' = \hat{\mathbf{x}}\hat{\mathbf{X}}^{-1}. \tag{32}$$

Proceeding in the same way, one describes the primary folding deformation of the second micro-triangle $\overset{\triangle}{023}$ forming $\mathcal{T}$. Fig. 11 shows two particular folded configurations of such elements. Upon introducing the second order rotation tensor $\mathbf{R}'$, which is represented by the matrix $\hat{\mathbf{R}}'$ in the Cartesian frame $\{\mathbf{e}_1, \mathbf{e}_2, \mathbf{e}_3\}$, we can write Eq. (31) into the following (absolute) vector form:

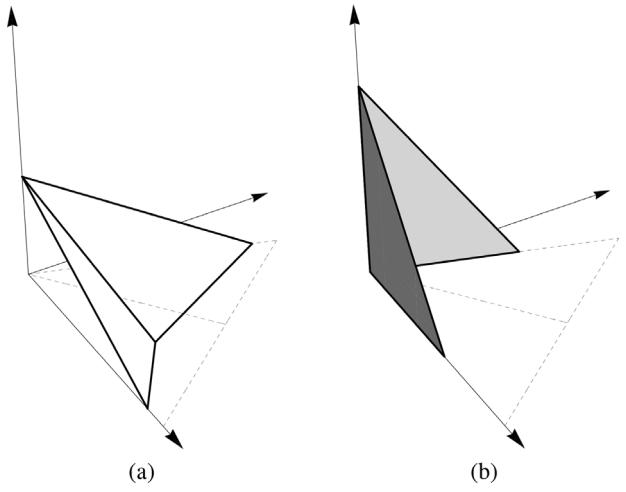

Fig. 11. (a) Partially folded (open) configuration of $\mathcal{T}$. (b) Fully folded configuration.

$$\mathbf{x}_i = \mathbf{x}_0 + \mathbf{R}'(\mathbf{X}_i - \mathbf{X}_0), \qquad (i = 1, 2). \tag{33}$$

5. Kinematics of the secondary folding motion

The secondary folding motion of the generic micro-triangle, say, e.g., the micro-triangle $\overset{\triangle}{023}$ shown in Fig. 12, carries the position vectors $\mathbf{x}_i$ into new position vectors $\mathbf{y}_i$ ($i = 0, 2, 3$), such that

$$\mathbf{y}_i = \mathbf{R}''\mathbf{x}_i, \tag{34}$$

$\mathbf{R}''$ denoting the tensor associated with a rotation of an angle θ about the axis $\mathbf{x}_3 - \mathbf{x}_0$ (Fig. 12). It is worth noting that $\mathbf{y}_0$ and $\mathbf{y}_3$, respectively, coincide with $\mathbf{x}_0$ and $\mathbf{x}_3$, for any value of θ, while $\mathbf{y}_2$ differs from $\mathbf{x}_2$,

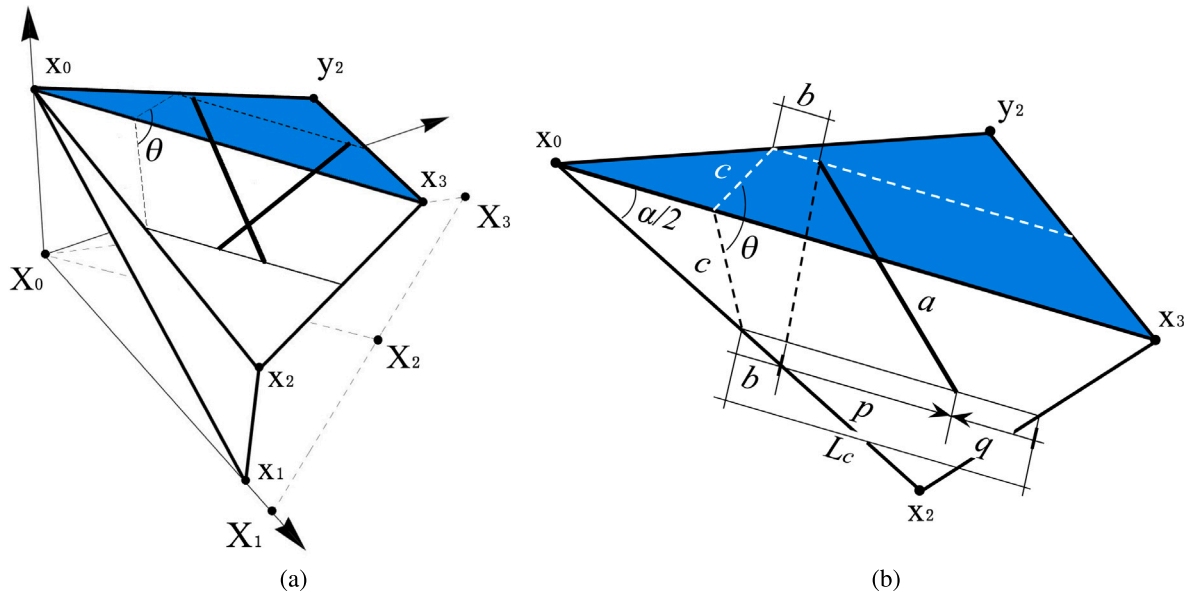

Fig. 12. Geometry of the secondary folding motion of the micro-triangle $\overset{\triangle}{023}$. (a) Global view. (b) Close-up of the folded plate.

for any $\theta \neq 0$. We now describe the deformation of the bars forming the scissor structure, which connects the supporting frame joining the points $\mathbf{x}_0$, $\mathbf{x}_2$ and $\mathbf{x}_3$ to the folded plate with vertices $\mathbf{y}_0$, $\mathbf{y}_2$ and $\mathbf{y}_3$. For the sake of simplicity, let us assume that the two bars of the scissor structure have negligible thickness and can be described as line segments. During the secondary folding motion, such members move symmetrically with respect to the normal to the base cable passing through its midpoint, and therefore the deformation law of the bar shown in Fig. 12(b) also fully determines the deformation law of the other bar. Let a, b, and c denote the length of the bar, the distance between the ball joint placed on top of the bar and the border of the folded micro-triangle (measured in the direction of the segment $\mathbf{x}_3$-$\mathbf{x}_0$), and the perpendicular distance between the segment $\mathbf{x}_3$-$\mathbf{x}_0$ and the base cable. The total length of the base cable is given by

$$L_c = L - \frac{2c}{\sin\alpha}\,. \tag{35}$$

In order to guarantee that the bar occupies a horizontal placement in the fully closed configuration of the micro-triangle, the variable a must satisfy the following limitation

$$a \leq L_c - b\,. \tag{36}$$

where we are assuming $b \ll L_c$. The current configuration of the bar under examination is described by the abscissa p of its bottom extremity measured along the base cable ('base coordinate'), which is shown in Fig. 12(b).

By simple geometry it is possible to write

$$a^2 - p^2 = 2c^2 - 2c^2(\cos\theta)\,, \tag{37}$$

which leads us to obtain p as a function of θ

$$p(\theta) = \sqrt{a^2 + 2c^2(\cos\theta - 1)}\,, \qquad \text{with} \quad -b \leq p \leq a\,. \tag{38}$$

In the fully closed configuration, it results in $\theta = 0$, implying $p = a$. Conversely, in the fully open configuration, it results in $p = 0$ (see Fig. 3, and Fig. S9), and one obtains the maximum folding angle $\theta_{\max}$ as follows:

$$\theta_{\max} = \arccos\left(1 - \frac{a^2}{2c^2}\right). \tag{39}$$

The above equation shows that it is possible to reach the desired value of $\theta_{\max}$ by suitably designing the values of a and c, making use of the formula

$$c = \frac{a}{\sqrt{2(1-\cos\theta_{\max})}}\,, \tag{40}$$

By inverting Eq. (38), we get

$$\theta(p) = \arccos\left(\frac{p^2 - a^2 + 2c^2}{2c^2}\right). \tag{41}$$

Fig. 13 plots the θ vs. p law given by Eq. (41), on considering $a = 1$ and different values of c.

We now compute the second base coordinate q shown in Fig. 12, obtaining

$$q = L_c - b - p\,, \qquad \text{with} \quad 0 \leq q \leq L_c\,. \tag{42}$$

By combining Eqs. (38) and (42), one determines q as a function of θ

$$q(\theta) = L_c - b - \sqrt{a^2 + c^2(\cos\theta - 1)}\,. \tag{43}$$

6. Stabilization of folding motions

The present section examines the response of the solar eye module when the system is stabilized by keeping the rest lengths of the cables fixed (activation winches/motors locked). We separately examine the stabilization of the primary and secondary folding motions in Sections 6.1 and 6.2, respectively. We compute the force–displacement response of a suitable portion $\mathcal{P}$ of the module when a time–history of a given displacement component is prescribed (always keeping the activation winches/motors in the locked position). In the case of the secondary folding motion, we validate the theoretical predictions against the results of experimental tests run on a physical model at the RPL of the University of Salerno (cf. Section 6.2). We wish to point out that the systems studied in the present work exclusively derive their stiffness properties from the elasticity of bars and cables, while the response of the systems studied in Miranda et al. (2020) is significantly influenced by the mechanical properties of the external actuators. The deformation of the structures analyzed hereafter is actually mainly due to the stretching of the cables, which are markedly more flexible than the bars.

Let $\mathbf{q}$ describe the vector collecting the free displacement components of the unconstrained nodes of $\mathcal{P}$ from a given reference configuration. Assuming that such nodes are not subject to external forces, we write the competent equilibrium equation as follows

$$g_r(\mathbf{q}) = \sum_{m=1}^{M} k_m\,(\ell_m(\mathbf{q}) - \bar{\ell}_m)\,\frac{\partial \ell_m}{\partial q_r} = 0\,, \tag{44}$$

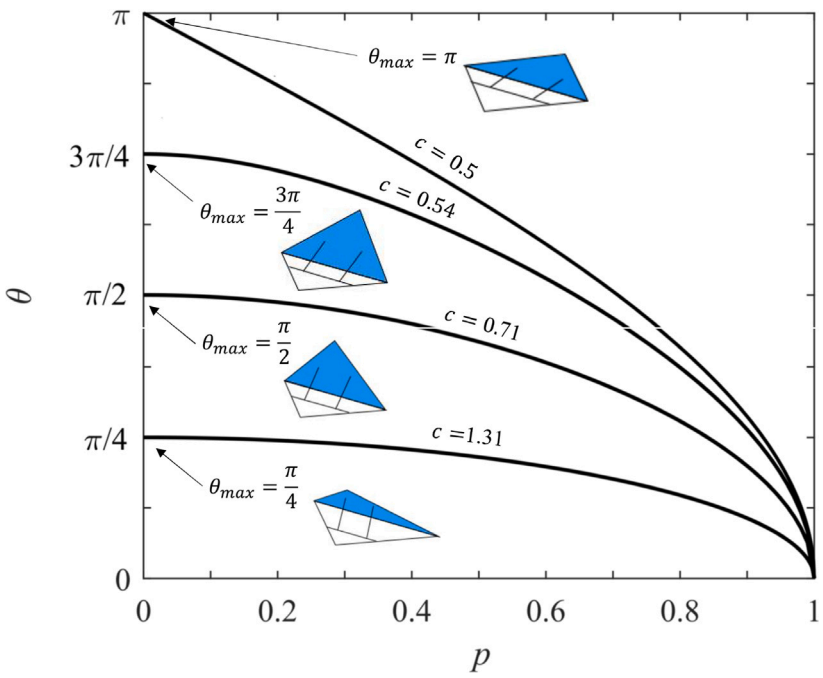

Fig. 13. Opening angle θ as a function of the base coordinate p, for $a = 1$ and different values of c. The insets show the configuration of the micro-triangle in the fully open placement ($\theta = \theta_{max}$).

where k_m is the stiffness coefficient of the generic bar or cable forming $\mathcal{P}$ ($m = 1, \ldots, M$); $\bar{\ell}_m$ is the rest length of such a member; ℓ_m is its deformed length; and q_r is the generic entry of $\mathbf{q}$ ($r = 1, \ldots, Q$) (Fraternali et al., 2015b). A deformation history of $\mathcal{P}$ is obtained by imposing that a given subvector $\mathbf{q}_p$ of $\mathbf{q}$ varies with time t according to a prescribed function $\mathbf{u}(t)$. The equilibrium problem of $\mathcal{P}$ can be solved by making use of the *extended system of equations* (Fraternali et al., 2015a)

$$\left\{ \begin{array}{c} \mathbf{g}(\mathbf{q}(t)) \\ \mathbf{q}_p - \mathbf{u}(t) \end{array} \right\} = \mathbf{0}, \tag{45}$$

$\mathbf{g}$ denoting the vector collecting all the *residuals* $g_1, \ldots, g_Q$.

It is useful to introduce a discretization of the deformation history into time steps $t_1, \ldots, t_S$. Examining the incremental equilibrium problem relative to the step $t_s \rightarrow t_{s+1}$, we let $\bar{\mathbf{q}}$ denote an initial guess of $\mathbf{q}(t_{s+1})$, which is such that it results in $\bar{\mathbf{q}}_p = \mathbf{u}(t_{s+1})$. We also set $\bar{\mathbf{g}} = \mathbf{g}(\bar{\mathbf{q}})$, and we introduce the subvectors $\mathbf{q}^a$ and $\mathbf{g}^a$, which are the complements of $\bar{\mathbf{q}}_p$ and $\bar{\mathbf{g}}_p$ with respect to $\bar{\mathbf{q}}$ and $\bar{\mathbf{g}}$, respectively. A correction $\boldsymbol{\Delta q}^a$ to $\bar{\mathbf{q}}^a$ is computed via the linear system of equations

$$\mathbf{K}^{T,aa}\, \boldsymbol{\Delta q}^a = -\mathbf{g}^a, \tag{46}$$

where $\mathbf{K}^{T,aa}$ is the submatrix of the *tangent stiffness matrix* with entries $K^T_{ij} = \partial g_i / \partial q_j$, which is associated to $\mathbf{g}^a$ and $\mathbf{q}^a$. We keep iterating the Newton–Raphson correction algorithm (46) until the norm of $\boldsymbol{\Delta q}^a$ gets lower than $10^{-6}\ \ell_{0_{min}}$, where $\ell_{0_{min}}$ is the minimum value of ℓ among all the members of $\mathcal{P}$ in the configuration at time $t = 0$.

6.1. Stabilization of the primary motion

Let us take the fully folded configuration ($\varepsilon = \varepsilon_{\max}$) of a right macro-triangle $\mathcal{P} \equiv \mathcal{T}$ as reference for a deformation ruled by a displacement history $u(t)$ of $\mathbf{x}_0$ along the $\mathbf{e}_3$ axis (Fig. 14). For $\alpha = \pi/2$ (right macro-triangle, see Fig. 8), such a process is assumed to take place while $\mathbf{x}_1$ is constrained to move along the $\mathbf{e}_1$ axis; $\mathbf{x}_3$ is constrained to move along the $\mathbf{e}_2$ axis; and the rest lengths of the opening and closing cables are kept fixed (Fig. 6).

We first consider a linear model of the response of $\mathcal{P}$, which is obtained by writing Eq. (46) at the initial time step ($t = t_1$).

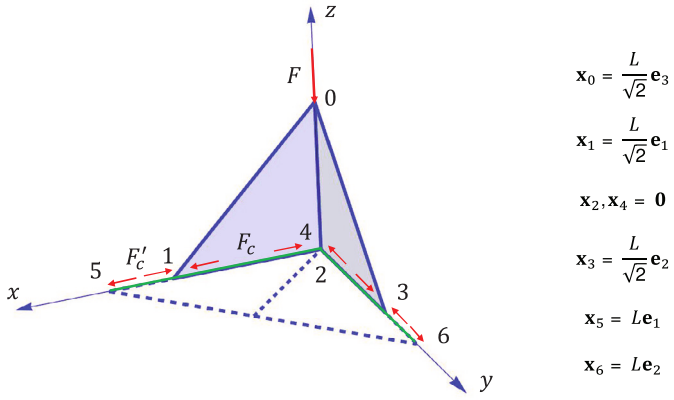

Fig. 14. Illustration of the mechanical model employed for the study of the stabilization of the primary folding motion.

Next, we predict the geometrically nonlinear response of $\mathcal{P}$ through a Mathematica® code that implements the path-following procedure described in the previous section.

Since we model a motion directed downward of $\mathbf{x}_0$, the opening cables are stretched during the deformation process under examination. In contrast, the closing cables are engaged only if they are preliminarily stretched through the application of a prestrain $p_0 = (\ell_0 - \bar{\ell})/\bar{\ell}$, which we assume is applied to both the opening and closing cables (through the bus cable). The closing cables remain active up to the time step in correspondence of which they become slack, due to the progressive increase of u. We let ℓ_0 and $\bar{\ell}$ respectively denote the lengths of the cables in the reference configuration and the rest configuration. The roles played by the opening and closing cables are reversed in correspondence to a deformation process that originates from the flat configuration and moves the vertex $\mathbf{x}_0$ upward. The opening cables connect the $\mathbf{x}_1$ and $\mathbf{x}_3$ nodes to a node $\mathbf{x}_4$ constrained to be at rest in correspondence to the projection of $\mathbf{x}_0$ onto the $\mathbf{e}_1$-$\mathbf{e}_2$ plane (Fig. 14).

The closing cables instead connect $\mathbf{x}_1$ and $\mathbf{x}_3$ to the nodes $\mathbf{x}_5$ and $\mathbf{x}_6$. The latter are at rest in correspondence to the vertices of $\mathcal{P}$ placed

$$\mathbf{K}^{T,0} = \frac{1}{L}\begin{pmatrix} \left(1+\sqrt{2}\right)B & \frac{B}{2} & 0 & 0 & -\sqrt{2}B & \frac{B}{2} \\ \frac{B}{2} & \left(\frac{1}{2}+\sqrt{2}\right)B+\sqrt{2}C & -\sqrt{2}B & 0 & 0 & 0 \\ 0 & -\sqrt{2}B & \sqrt{2}B & 0 & 0 & 0 \\ 0 & 0 & 0 & \sqrt{2}B & 0 & -\sqrt{2}B \\ -\sqrt{2}B & 0 & 0 & 0 & \sqrt{2}B & 0 \\ \frac{B}{2} & 0 & 0 & -\sqrt{2}B & 0 & \left(\frac{1}{2}+\sqrt{2}\right)B+\sqrt{2}C \end{pmatrix} \tag{51}$$

Box I.

along the x ad y axes in the fully open configuration. The application of a prestrain p_0 to the opening and closing cables induces the following pre-tensioning forces F_c and F_c' in these members (Fig. 14)

$$F_{c_p} = F'_{c_p} = (EA)_c\, p_0\,, \tag{47}$$

where $(EA)_c$ is the axial stiffness of the cables (i.e., the product of the Young modulus of the material times the cross-section area). The bars shown in Fig. 14 describe the supports of the plates that form the micro-triangles of $\mathcal{P}$ (see Fig. S7 of Supplementary Materials), and are assumed to exhibit an axial stiffness $(EA)_b$. Let u_{x_i}, u_{y_i}, u_{z_i} denote the Cartesian components of the displacement of the generic node $\mathbf{x}_i$ from the reference configuration of Fig. 14. The vector of the nonzero displacement components of the system under consideration is given by $\mathbf{q} = \{u_{z_0}, u_{x_1}, u_{x_2}, u_{y_2}, u_{z_2}, u_{y_3}\}$.

6.1.1. Linearized response

We now examine the case with $p_0 = 0$ ($F_c' = 0$). It is easily verified that, in this case, the equilibrium equations of the system in Fig. 14 can be written as follows

$$\mathbf{g} = \mathbf{A}\mathbf{f} - \mathbf{w} = \mathbf{0}\,, \tag{48}$$

where $\mathbf{f}$ is the vector of the axial forces in the members 1–4, 3–4, 0–1, 1–2, 0–2, 0–3, 2–3 (assumed positive in tension); $\mathbf{w}$ is the vector of the external nodal forces; and $\mathbf{A}$ is the equilibrium matrix given by

$$\mathbf{A} = \begin{pmatrix} 0 & 0 & \frac{1}{\sqrt{2}} & 0 & 1 & \frac{1}{\sqrt{2}} & 0 \\ \frac{1}{\sqrt{2}} & 0 & \frac{1}{\sqrt{2}} & 1 & 0 & 0 & 0 \\ 0 & 0 & 0 & -1 & 0 & 0 & 0 \\ 0 & 0 & 0 & 0 & 0 & 0 & -1 \\ 0 & 0 & 0 & 0 & -1 & 0 & 0 \\ 0 & \frac{1}{\sqrt{2}} & 0 & 0 & 0 & \frac{1}{\sqrt{2}} & 1 \end{pmatrix}. \tag{49}$$

The introduction of elastic constitutive equations in the cables and bars leads us to write

$$\begin{aligned} f_1 &= k_c\left(\|(\mathbf{x}_1 + q_2\,\mathbf{e}_1) - \mathbf{x}_4\| - \bar{\ell}_{1,4}\right), \\ f_2 &= k_c\left(\|(\mathbf{x}_3 + q_6\,\mathbf{e}_2) - \mathbf{x}_4\| - \bar{\ell}_{3,4}\right), \\ f_3 &= k_b\left(\|(\mathbf{x}_0 + q_1\,\mathbf{e}_3) - (\mathbf{x}_1 + q_2\,\mathbf{e}_1)\| - \bar{\ell}_{0,1}\right), \\ f_4 &= k_b\left(\|(\mathbf{x}_1 + q_2\,\mathbf{e}_1) - (\mathbf{x}_2 + q_3\,\mathbf{e}_1 + q_4\,\mathbf{e}_2 + q_5\,\mathbf{e}_3)\| - \bar{\ell}_{1,2}\right), \\ f_5 &= k_b\left(\|(\mathbf{x}_0 + q_1\,\mathbf{e}_3) - (\mathbf{x}_2 + q_3\,\mathbf{e}_1 + q_4\,\mathbf{e}_2 + q_5\,\mathbf{e}_3)\| - \bar{\ell}_{0,2}\right), \\ f_6 &= k_b\left(\|(\mathbf{x}_0 + q_1\,\mathbf{e}_3) - (\mathbf{x}_3 + q_6\,\mathbf{e}_2)\| - \bar{\ell}_{0,3}\right), \\ f_7 &= k_b\left(\|(\mathbf{x}_2 + q_3\,\mathbf{e}_1 + q_4\,\mathbf{e}_2 + q_5\,\mathbf{e}_3) - (\mathbf{x}_3 + q_6\,\mathbf{e}_2)\| - \bar{\ell}_{2,3}\right), \end{aligned} \tag{50}$$

with $k_c = (EA)_c/\bar{\ell}_c$ and $k_b = (EA)_b/\bar{\ell}_b$, where $\bar{\ell}_c$ and $\bar{\ell}_b$ denote the rest lengths of the current cable and bar, respectively. The use of Eqs. (50) into (48) leads us to compute the tangent stiffness matrix of the system $\mathbf{K}^{T,0} = \{\partial g_i/\partial q_j\}$ in correspondence to the reference configuration of Fig. 14, obtaining Eq. (51) (see Box I) with $B = (EA)_b$ and $C = (EA)_c$.

Assuming small displacements from the reference configuration, we now transform the equilibrium problem (48) into the following linear elastic problem

$$\mathbf{K}^{T,0}\,\mathbf{q} = \mathbf{w}\,. \tag{52}$$

In the limit $B \to \infty$, we obtain the following solution

$$\mathbf{q}^0 = \frac{F\,L}{2\sqrt{2}C}\,\{-1, 1, 1, 1, -1, 1\} \tag{53}$$

for the case of a single vertical force F applied to node $\mathbf{x}_0$ (pointing downward). In correspondence to the same loading condition, we also to predict that the force acting in the opening cables is equal to

$$F_c^0 = \frac{F}{2}\,. \tag{54}$$

Let $F_{c,f}$ denote the breaking force of the cables. According to Eq. (54), the value F_f of F that produces the breakage of the cables should be equal to $2\,F_{c,f}$. We will see in the next section, however, that the F_c/F ratio significantly grows with the magnitude of displacements exhibited by the structure from the reference configuration. Such a phenomenon may cause the failure of the strings for values of F significantly lower than $2\,F_{c,f}$.

6.1.2. Response in the large displacement regime

The present section examines the response of the macro-triangle $\mathcal{P}$ shown in Fig. 14 in the large displacement regime, making use of the path-following procedure in displacement control illustrated in Section 6. We assume that the vector $\mathbf{q}_p$ is composed of the single entry $u_p \equiv u_{z_0}$, which is prescribed to vary with time according to a linear time history $u(t)$, which features $u = 0$ at the initial time step and $u = u_{\max} = \sqrt{\varepsilon_{\max}\left(2-\varepsilon_{\max}\right)}L = L/\sqrt{2}$ at the final step (cf. Section 5). The employed numerical model makes use of the geometry and members' sizes of a simplified version of the small-scale mock-up analyzed in Section 3 and Supplementary Materials, being formed by two isosceles right micro-triangles with hypotenuse length $L = 183$ mm. This model will be employed as a portion of a quadrangular module in Section 7. The opening and closing cables are made of monofilament nylon fishing line wire with a 0.40 mm diameter, 1.0 MPa Young modulus and $F_{c,f} = 21.57\ N$ breaking force. The bars forming the system are instead made of steel with 210 GPa Young modulus, and exhibit a 3 mm × 5 mm rectangular cross section. Fig. 15(a) shows the predicted force F vs. displacement u response of the macro-triangle, in correspondence to different values of the prestrain p_0 (a time history with 5000 steps was employed to construct such curves). The force F was identified with the quantity g_p that is associated to u_p through Eq. (44). The plot in Fig. 15(a) relates F to the breaking force of the cables $F_{c,f}$, and refers the displacement u to the stroke $u_{\max}$. The dashed portions of the curves labeled (*ii*) in Fig. 15(a) are theoretical, since they correspond to forces in the cables greater than the breaking force $F_{c,f}$. The portions labeled (*i*) instead correspond to cable forces not greater than the breaking force $F_{c,f}$. Panel (b) of Fig. 15 shows a deformed configuration of the system, while panel (c) gives the plot of the F_c/F ratio when $u/u_{\max}$ varies from 0 to 0.8.

The plots given in Fig. 15(a) highlight that the $F-u$ curve exhibits a slope (i.e., a tangent stiffness) that progressively reduces in amplitude for growing values of u. It would theoretically lead the system to a limit-point-buckling mode (Budiansky, 1974), if the cables exhibit a sufficiently large breaking force. The value of the force F corresponding

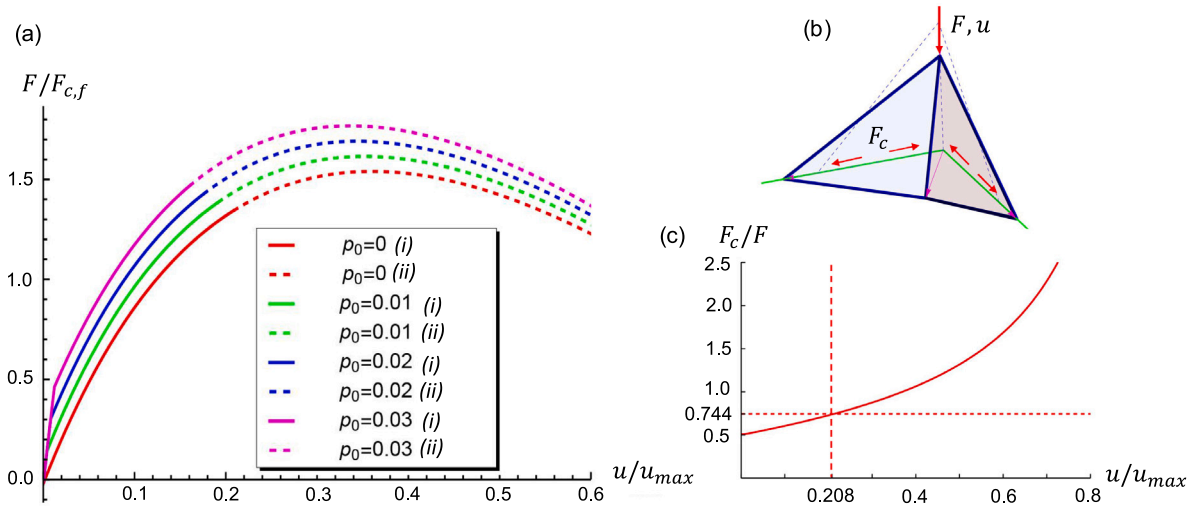

Fig. 15. (a) Numerical results for the curves relating $F/F_{c,f}$ to u/u_{umax} in correspondence to the stabilization of the primary folding motion of a reduced scale mock-up of a macro-triangle, at varying values of the cable prestrain p_0. The solid (*i*) portions of the $F-u$ curves refer to the actual response branches, since along such branches the cables are loaded by tensile forces lower than the breaking load $F_{c,f}$. The dashed potions (*ii*) are instead theoretical, since they refer to values of F that induce forces in the cables above the breaking load. (b) Deformed configuration of the system. (c) Plot showing the variation of the F_c/F ratio with the vertical displacement of the top node, for $p_0 = 0$.

to such a buckling event is hereafter referred to as F_l. The results presented in Fig. 15(a) show that the condition $F = F_l$ occurs for $u = u_l$ varying from 0.34 $u_{\max}$ ($p_0 = 0$) to 0.36 $u_{\max}$ ($p_0 = 0.03$). This means that the buckling event takes place at about 1/3 of the stroke of the top vertex $\mathbf{x}_0$. The results in Fig. 15(a) also indicate that the $F-u$ curves slightly move upward for growing values of p_0, due to the presence of stiff branches near $u = 0$, which are induced by the initial engagement of the closing cables, for nonzero values of p_0. In the case of the mock-up under examination, F_f assumes the values of 1.34 $F_{c,f}$ (at $u = 0.208\ u_{\max}$) and 1.46 $F_{c,f}$ (at $u = 0.160\ u_{\max}$) respectively for $p_0 = 0$ and $p_0 = 3\%$. Similarly, in the same model, F_l assumes the values of 1.54 $F_{c,f}$ and 1.77 $F_{c,f}$ for $p_0 = 0$ and $p_0 = 3\%$, respectively. It is worth noting that the above values of the $F_f/F_{c,f}$ ratio are significantly lower than the value of 2 predicted by the linear analysis presented in the previous section. For $p_0 = 0$, the plot given in Fig. 15(c) indeed shows that the ratio between the force F_c acting in the opening cables and the external force F markedly grows above 0.5 for u slightly larger than zero, and that such a ratio assumes the value 0.744 at $u = 0.208\ u_{\max}$.

If the external loads applied to $\mathcal{P}$ (typically wind forces (Miranda et al., 2020)) are expected to produce forces in the cables greater than F_f, one should adopt suitable protection strategies of the solar module, by using, e.g., motion stoppers formed by springs with suitable rest lengths, which are placed at the extremities of the sliding tracks shown in Fig. 6 (see also Supplementary Materials).

6.2. Stabilization of the secondary motion

We conducted a numerical study on the stabilization of the secondary folding motion on a physical model of a micro-triangle, which retains the main features of the micro-triangles of the demonstrative mock-up (cf. Section 3 and Supplementary Materials). Our theoretical predictions were validated against experimental tests conducted at the RPL of the University of Salerno.

6.2.1. Physical model and experimental setup

Let us analyze the micro-triangle shown in Fig. 16, which exhibits the following geometrical properties, using the symbols introduced in Section 5: $a = 60$ mm, $b = 0$ mm, $c = 41.05$ mm, $L/\sqrt{2} = 116.14$ mm. A physical sample was built with such a geometry, using a support frame with 3 mm × 5 mm rectangular cross-section bars, and the

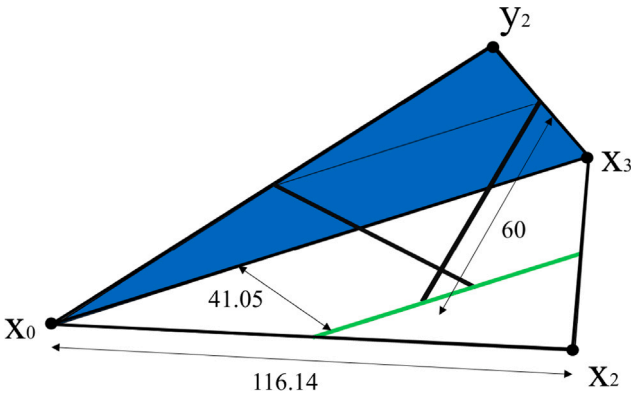

Fig. 16. Geometry of the tested sample of a micro-triangle (dimensions in mm).

pins of the scissor structure showing 2.8 mm × 1.5 mm rectangular cross-section. Such members where 3D printed in 'Matte Black Steel' by Shapeways®(210 GPa Young modulus). The foldable plate was 3D printed in gray ABS at RPL with 3 mm thickness. We used ABS instead of Matte Black Steel for this element to reduce its mass, which is not taken into consideration in the simulations presented hereafter. The pins of the scissor structure are connected to a looped bus cable made of a nylon wire with 0.4 mm diameter, which is identical to that mentioned in the previous section.

The supporting frame was screwed to an optical table and a loading test was run to measure the stiffness of the system in the stabilized configuration. The latter was obtained by constraining the rest length of the bus cable, which was also screwed against the supporting frame. We measured the variation Δd of the distance d between the nodes $\mathbf{y}_2$ and $\mathbf{x}_2$ shown in Fig. 16, due to the application of a loading condition that produces the progressive closure of the foldable plate. Such a plate was assumed to occupy an initially folded configuration forming an angle of 52 deg with the horizontal plane, before the application of the external load. We let d_0 denote the value of d in correspondence to such a configuration. The base cables were prestressed by connecting them to two external baskets loaded with calibration weights ('prestress baskets'). The connection between each cable and the corresponding

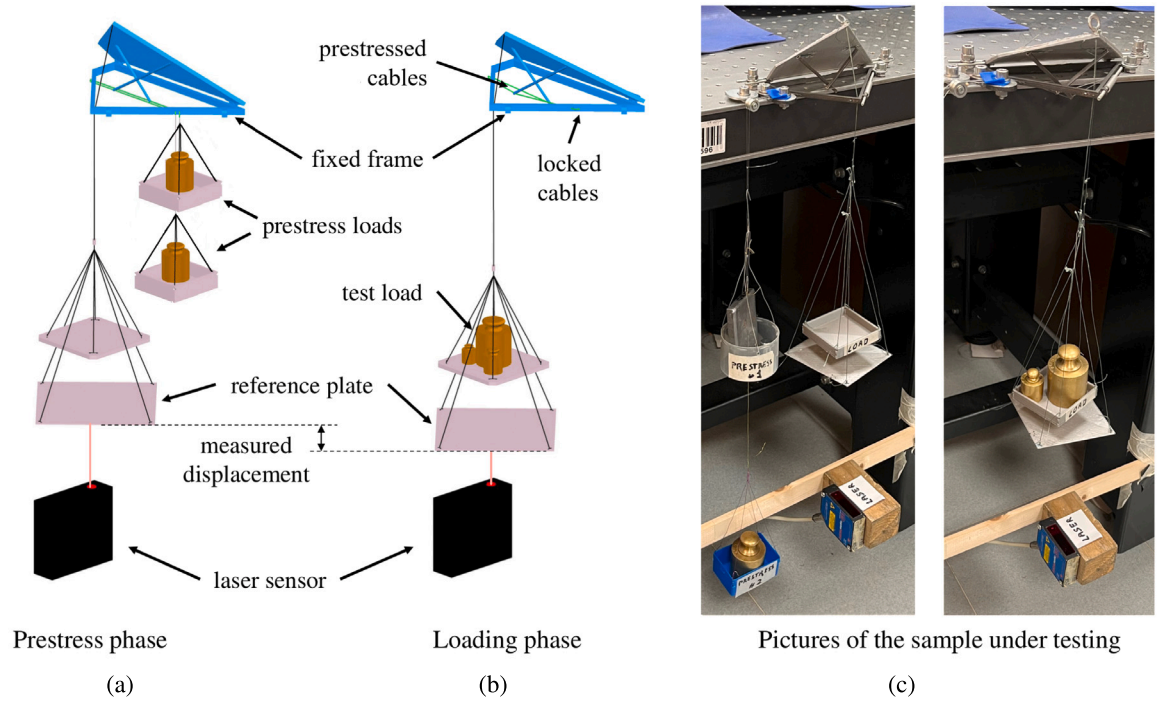

Fig. 17. Illustrative scheme of the loading test carried out on a reduced scale micro-triangle (a–b), and pictures of the physical sample under testing (c).

prestress basket was realized through metallic bars with 1 mm diameter forming a pyramid structure (Fig. 17(a)). Two values of the loads on the prestress basket were analyzed: $F_{c,p} = 250$ gf and $F_{c,p} = 500$ gf. By referring the above values of the prestress force $F_{c,p}$ to the breaking force of the cables $F_{c,f} = 21.57$ N, we obtain $F_{c,p} = 0.114\ F_{c,f}$ and $F_{c,p} = 0.227\ F_{c,f}$, respectively. As anticipated, after applying the prestress load, the rest lengths of the base cables were locked (by screwing them against the supporting frame) and the prestress load baskets were removed (Fig. 17(b)). Next, the $\mathbf{y}_2$ node was loaded by applying calibration weights on a 'loading basket' connected to $\mathbf{y}_2$ through a PowerPro® braided Spectra fiber with 0.76 mm passing through the supporting frame, as shown in Fig. 17. The total weight applied to the loading basket is transferred to $\mathbf{y}_2$ through a force F acting in the Spectra cable. We measured the displacement $\Delta d = d_0 - d$ by recording the variation of the vertical position of the reference plate attached to the loading basket, through a laser sensor (Fig. 17(a,b)). We applied calibration weights on the loading basket with steps of 20/50 g, and we recorded the vertical position of the loading plate at the end of each loading step. A picture of the physical sample under testing is shown in Fig. 17(c).

6.2.2. Mechanical model and force–displacement response

We introduced the mechanical model shown in Fig. 18(a) to predict the response of the physical model described in Section 6.2.1. The panels (b) and (c) of this figure illustrate two configurations of the physical model under testing. We let $\mathbf{x}_i$ and $\mathbf{y}_i$ indicate the position vectors occupied by the nine nodes shown in Fig. 18(a) in the reference and the deformed configurations, respectively (see Supplementary Materials for the expressions of the $\mathbf{x}_i$ vectors). The nodes 0–4 are at rest during the deformation under consideration ($\mathbf{y}_i \equiv \mathbf{x}_i$), while the nodes 5–7 exhibit a rotation about the x-axis of angle θ variable from 52 deg (reference configuration) through zero, which implies

$$\begin{pmatrix} y_{x_i} \\ y_{y_i} \\ y_{z_i} \end{pmatrix} = \begin{pmatrix} 1 & 0 & 0 \\ 0 & \cos\theta & -\sin\theta \\ 0 & \sin\theta & \cos\theta \end{pmatrix} \begin{pmatrix} X_{x_i} \\ X_{y_i} \\ X_{z_i} \end{pmatrix}, \quad (i = 5, 6, 7) \tag{55}$$

X_{x_i}, X_{y_i} and X_{z_i} denoting the Cartesian coordinates of the ith node in the fully closed configuration ($\theta = 0$). The Cartesian components of the displacements of nodes 5–9 form the vector $\mathbf{q}$ of the nonzero displacements, while the displacement components of nodes 5–7 form the subvector of the prescribed displacements $\mathbf{q}_p$. Finally, the displacement components of nodes 8 and 9 form the subvector $\mathbf{q}^a = \{u_{x_8}, u_{y_8}, u_{z_8}, u_{x_9}, u_{y_9}, u_{z_9}\}$. The deformable members of the system in Fig. 18(a) are the cables 8–4, 8–3, 9–3, 9–4, and the bars 6–9 and 7–8. The remaining elements undergo rigid body motions or stay at rest during the deformation process under consideration. The cables 8–4 and 8–3 are overlapped to the cables 9–4 and 9–3 in the reference configuration, but it is worth noting that such members form two separate sets of elements that exhibit different deformed configurations. In the physical model the same cables are slightly offset in the y-direction, as shown in Figs. 18(b),(c). The problem to be considered for the computation of $\mathbf{q}^a$ is formed by the equilibrium equations of nodes 8–9, which are written as follows

$$\mathbf{g}_8 = f_{3,8}\frac{\mathbf{y}_3 - \mathbf{y}_8}{\ell_{3,8}} + f_{0,8}\frac{\mathbf{y}_0 - \mathbf{y}_8}{\ell_{0,8}} + f_{7,8}\frac{\mathbf{y}_7 - \mathbf{y}_8}{\ell_{7,8}} = \mathbf{0}, \tag{56}$$

$$\mathbf{g}_9 = f_{0,9}\frac{\mathbf{y}_0 - \mathbf{y}_9}{\ell_{0,9}} + f_{3,9}\frac{\mathbf{y}_3 - \mathbf{y}_9}{\ell_{3,9}} + f_{6,9}\frac{\mathbf{y}_6 - \mathbf{y}_9}{\ell_{6,9}} = \mathbf{0}, \tag{57}$$

where $f_{i,j}$ and $\ell_{i,j}$ denote the axial force and the current length of the member joining nodes i and j, respectively. By grouping the above equilibrium equations, we write

$$\mathbf{g} = \begin{Bmatrix} \mathbf{g}_8 \\ \mathbf{g}_9 \end{Bmatrix} = \mathbf{0}. \tag{58}$$

Let us now make use of the constitutive equations $f_{i,j} = k_{i,j}(\|\mathbf{y}_i - \mathbf{y}_j\| - \bar{\ell}_{i,j})$, with $k_{i,j} = (EA)_c/\bar{\ell}_c$ in the cables and $k_{i,j} = (EA)_b/\bar{\ell}_b$ in the bars. On accounting for such relations and Eqs. (55), we are able to express the residual vector $\mathbf{g}$ as a function of $\mathbf{q}$. Due to the nonlinear nature of the resulting system of Eqs. (58), we employ the path-following procedure presented in Section 6 for its solution. We apply a displacement history that lets θ linearly decrease from 52 deg to zero through 100 steps of 5.2 deg each.

At the end of each time step, we compute the current value of the force F acting on node 5, by setting to zero the resultant moment of the external forces acting on the micro-triangle $\overset{\triangle}{015}$ about the support

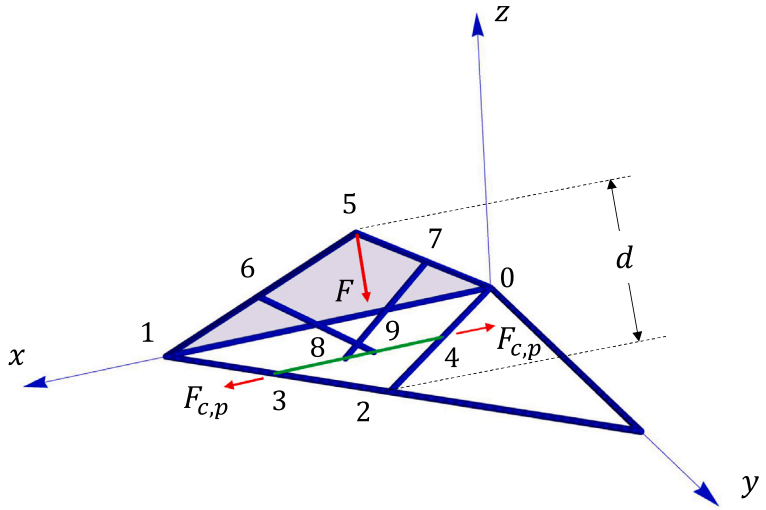

(a)

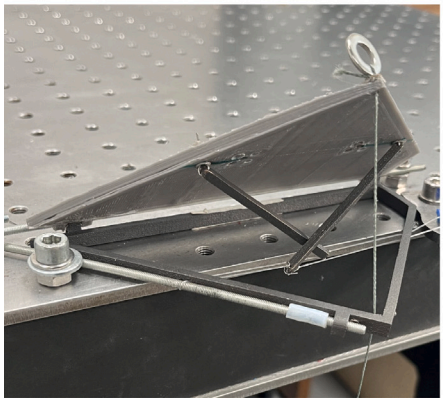

(b)

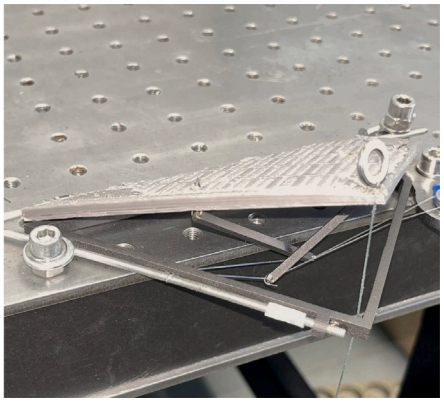

(c)

Fig. 18. Illustration of the mechanical and physical models employed for the study of the stabilization of the secondary folding motion. (a) Reference configuration of the mechanical model (see Supplementary Materials for the node coordinates). (b) Close-up picture of the reference configuration of the physical sample. (c) Deformed configuration of the physical sample under testing.

axis 0–1. Such an equation is written as follows

$$\left((\mathbf{y}_6 - \mathbf{y}_0) \times f_{6,9} \, \frac{\mathbf{y}_6 - \mathbf{y}_9}{\ell_{6,9}} \; + \; (\mathbf{y}_7 - \mathbf{y}_0) \times f_{7,8} \, \frac{\mathbf{y}_7 - \mathbf{y}_8}{\ell_{7,8}} \right.$$
$$\left. - \; (\mathbf{y}_5 - \mathbf{y}_0) \times F \, \frac{\mathbf{y}_5 - \mathbf{y}_2}{\ell_{5,2}} \right) \cdot \mathbf{e}_1 \; = \; 0 \, . \tag{59}$$

Panel (a) of Fig. 19 shows a comparison between predicted (numerical) and experimental $F/F_{c,f}$ vs. $\Delta d/d_0$ curves obtained for the examined values of the prestress force $F_{p,c}$.

As in the case of the stabilization of motion 1, we use dashed lines to mark the portions (*ii*) of the $F - d$ curves that correspond to forces in the cables greater than $F_{c,f}$. Panel (b) of Fig. 19 shows a deformed configuration of the system under study, while panel (c) illustrates the variation of the force ratio F_c/F with the displacement variable $\Delta d/d_0$, for $F_p = 0.114 \; F_{c,f}$. Here F_c denotes the maximum axial force acting in the cable elements. We observe the presence of a stiffening-type response branch of the $F - \Delta d$ curve (tangent stiffness increasing with increasing values of the displacement control variable) for small values of Δd, which is followed by a softening branch.

The numerical model predicts the occurrence of a limit-point buckling mode at the end of such a softening phase, similarly to what we observed in the previous section (it is worth remarking that the experimental tests were conducted in force control, while the numerical simulations were run in displacement control). In the present case, such an event would occur for $\Delta d/d_0 \approx 1$ ($\theta \approx 0$). The results given in Fig. 19(a) show that the theoretical predictions of the force–displacement response match the experimental results rather well. For $F_p = 0.114 \; F_{c,f}$ the numerical model predicts the achievement of the failure load $F_f = 0.438 \; F_{c,f}$ at 68% of the stroke that takes d to zero. Differently, for $F_p = 0.227 \; F_{c,f}$, the numerical model predicts $F_f = 0.432 \; F_{c,f}$ at 61% of the stroke. The plot in Fig. 19(c) shows that the ratio between the maximum force in the cables F_c and the external force F is initially rather high, for small displacements and small values of F, and next decreases down to values comprised in the range [2.28,2.40], for Δd varying from 50% to 80% of the stroke (assuming $F_p = 0.114 \; F_{c,f}$).

If, in the event of extreme loading conditions, the forces applied to the system are expected to overcome the failure load of the cables (due, e.g., to high winds), one can protect the folded micro-triangles by closing them, like in the case of retractable awnings equipped with anemometers (Goodman and Meier, 2013).

7. Dynamic response and wind loading

Let us analyze the dynamic response of the quadrilateral system shown in Fig. 20, which occupies a semi-closed configuration of the solar eye ($\varepsilon = 0.5 \; \varepsilon_{\max}$). Such a configuration is hereafter assumed as reference for a study of the effects of upwind loading, which considers the wind acting perpendicular to the base of the module (i.e., wind loading perpendicular to a building façade/rooftop equipped with solar

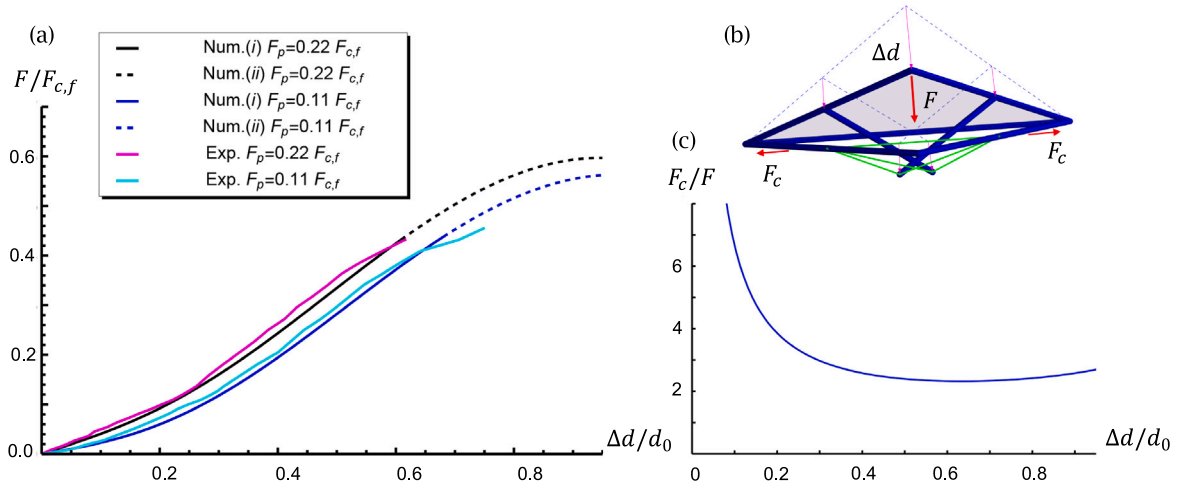

Fig. 19. (a) Comparison between theoretical predictions and experimental observations of the force–displacement curve analyzed for the stabilization of the secondary folding motion, for different values of the prestress force F_p in the base cable. (b) Deformed configuration of the system. (c) Plot showing the variation of the F_c/F ratio with $\Delta d/d_0$, for $F_p = 0.113\ F_{c,f}$.

eyes). The reason for this choice is that the semi-closed configuration is more exposed to the analyzed loading condition, as compared to the fully open and fully closed configurations of the solar eye. One easily realizes, indeed, that the fully open (or fully folded) configuration analyzed in Section 6.1 shows a reduced (theoretically zero) projected surface area under upwind loading, while the fully closed configuration is protected by the supporting frame against wind-induced vibrations (cf. Figs. 6–7). Assuming the action of high or moderately high winds, we safely suppose that the secondary folding motion of the micro-triangles is not active (see our considerations at the end of the previous section). Upwind loading tends to produce a downward displacement of the central node 0 of the system in Fig. 20 (i.e., a negative displacement component of this node along the z-axis). We therefore equip our mechanical model with only the opening cables 1–4, 3–4, 6–4, 8–4, and suppose that the closing cables are not reactive, due to the absence of prestress. An opposite situation (closing cables active and opening cables not reactive) should be considered in the presence of a downwind loading condition, assuming again, for simplicity, zero prestress of the cables. The vectors of the coordinates of the vertices of the macro-triangle 0-1-2-3 are given by

$$\begin{aligned}
\mathbf{x}_0 &= \left\{0,\, 0,\, \frac{1}{2}\sqrt{\frac{5}{2}-\sqrt{2}}L\right\},\\
\mathbf{x}_1 &= \left\{\frac{1}{4}\left(2+\sqrt{2}\right)L,\, 0,\, 0\right\},\\
\mathbf{x}_2 &= \left\{\frac{L}{4+\sqrt{2}},\, \frac{L}{4+\sqrt{2}},\, -\frac{\sqrt{5-2\sqrt{2}}L}{8+2\sqrt{2}}\right\},\\
\mathbf{x}_3 &= \left\{0,\, \frac{1}{4}\left(2+\sqrt{2}\right)L,\, 0\right\},
\end{aligned} \tag{60}$$

and it is not difficult to generalize the above equations to obtain the position vectors of the remaining nodes shown in Fig. 20. The node 4 is at rest in correspondence to the origin of the global Cartesian frame x, y, z.

We wish to study the dynamic response of the system shown in Fig. 20 under small, wind-induced vibrations from the reference configuration. The vector of the free displacement components $\mathbf{q}$ is formed in the present case by the vertical displacement component of node 0; the displacement components along the x-axis of nodes 1 and 6; the displacement components along the y-axis of nodes 3 and 8, and the displacement components along the x, y, z axes of nodes 2, 5, 7 and 9, for a total of 17 kinematic variables. The tangent stiffness matrix of the system in the reference configuration (i.e., the matrix $\mathbf{K}^{T,0}$) is given by the assembly of the $\mathbf{K}^{T,e}$ matrices of the four macro-triangles shown in Fig. 20. Let $\mathbf{q}^1 = \{u_{z_0}, u_{x_1}, u_{x_2}, u_{y_2}, u_{z_2}, u_{y_3}\}$ denote the vector of kinematic variables pertaining to the 0-1-2-3 macro-triangle. Making use of an approach similar to that followed in Section 6.1.1, it is easily shown that the matrix $\mathbf{K}^{T,1}$ of such an element has the following expression

$$\mathbf{K}^{T,1} = \frac{1}{L}\begin{pmatrix}
k_{11} & k_{12} & k_{13} & k_{14} & k_{15} & k_{16}\\
 & k_{22} & k_{23} & k_{24} & k_{25} & k_{26}\\
 & & k_{33} & k_{34} & k_{35} & k_{36}\\
 & Sym & & k_{44} & k_{45} & k_{46}\\
 & & & & k_{55} & k_{56}\\
 & & & & & k_{66}
\end{pmatrix}, \tag{61}$$

where

$$\begin{aligned}
k_{11} &= \frac{1}{196}\left(309+26\sqrt{2}\right)B,\\
k_{12} &= k_{16} = \frac{1}{8}\sqrt{7+4\sqrt{2}}B,\\
k_{13} &= k_{14} = \frac{1}{49}\sqrt{430-104\sqrt{2}}B,\\
k_{15} &= -\frac{1}{49}\left(16+31\sqrt{2}\right)B,\\
k_{22} &= k_{66} = \frac{1}{392}\left(363+296\sqrt{2}\right)B - \left(2\sqrt{2}-4\right)C,\\
k_{23} &= k_{46} = -\frac{1}{196}\left(108+99\sqrt{2}\right)B,\\
k_{24} &= k_{36} = \frac{1}{98}\left(30+3\sqrt{2}\right)B,\\
k_{25} &= k_{56} = -\frac{1}{392}\sqrt{645-156\sqrt{2}}B,\\
k_{26} &= 0,\\
k_{33} &= k_{44} = \frac{1}{196}\left(44+171\sqrt{2}\right)B,\\
k_{34} &= \frac{1}{49}\left(6\sqrt{2}-38\right)B,\\
k_{35} &= k_{45} = -\frac{1}{192}\sqrt{2351-1328\sqrt{2}}B,\\
k_{55} &= \frac{1}{98}\left(123\sqrt{2}-44\right)B.
\end{aligned} \tag{62}$$

Here the symbols B and C have the same meaning introduced in Section 6.1.1. The $\mathbf{K}^{T,e}$ matrices of the three remaining macro-triangles have expressions identical to $\mathbf{K}^{T,1}$ with respect to the corresponding

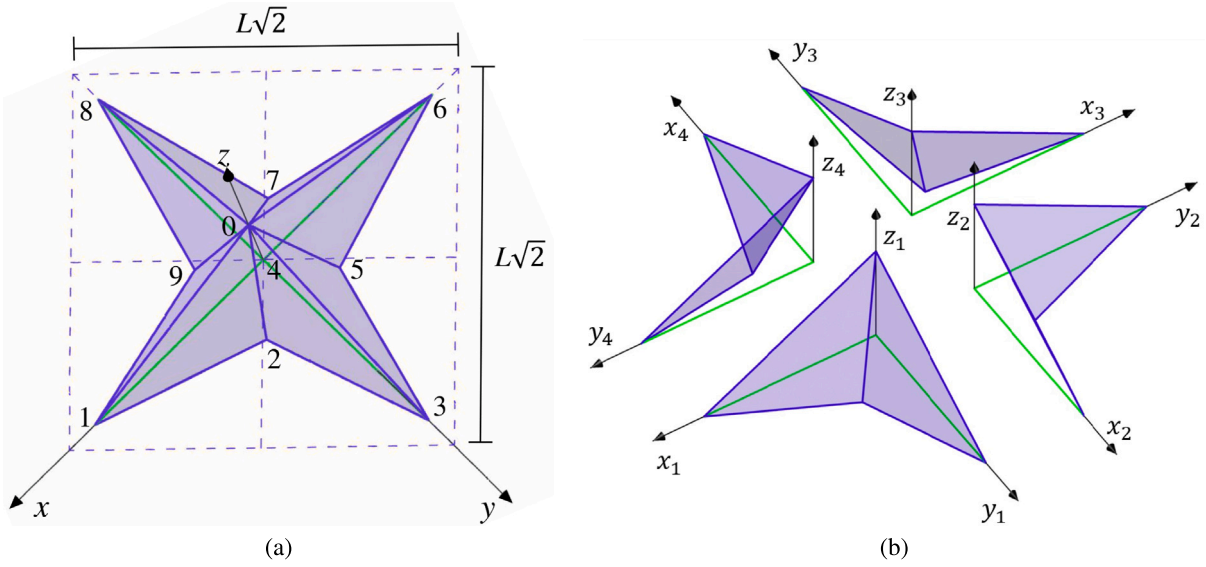

Fig. 20. (a) Three-dimensional view of the mechanical model of a quadrilateral system. (b) Disassembling of the system into four macro-triangles.

local Cartesian frames $\{x_i, y_i, z_i\}$ (see Fig. 20(b)). Passing on to analyze the mass matrix of the system, we let m denote the overall mass of a micro-triangle. We lump such a mass in correspondence to the vertices of this element, which leads us to consider the following mass matrix of the generic macro-triangle

$$\mathbf{M}^e = \frac{1}{3}\, m \begin{pmatrix} 2 & 0 & 0 & 0 & 0 & 0 \\ 0 & 1 & 0 & 0 & 0 & 0 \\ 0 & 0 & 2 & 0 & 0 & 0 \\ 0 & 0 & 0 & 2 & 0 & 0 \\ 0 & 0 & 0 & 0 & 2 & 0 \\ 0 & 0 & 0 & 0 & 0 & 1 \end{pmatrix}. \tag{63}$$

The assembling of the element matrices $\mathbf{M}^e$ gives rise to the global mass matrix $\mathbf{M}$. The free vibration problem of the structure shown in Fig. 20 is studied via modal analysis, making use of the eigenvalue problem

$$\mathbf{K}^{T,0}\, \boldsymbol{\Phi} = \mathbf{M}\, \boldsymbol{\Phi}\, \boldsymbol{\Omega}^2, \tag{64}$$

where $\boldsymbol{\Omega}^2$ is the diagonal matrix collecting the squares ω_i^2 of the angular vibration frequencies of the single modes, and $\boldsymbol{\Phi}$ is the matrix of the vibration modes (see, e.g., Bathe and Wilson (1973)). We agree to order the modes by increasing values of the vibration frequencies.

We now analyze the special case of the reduced scale mock-up of the solar eye, assuming $L = 183$ mm and considering the member properties that have been illustrated in Section 6.1.2. In addition, we suppose $m = 0.197$ kg, which corresponds to the mass of an isosceles right micro-triangle made of steel with hypotenuse length $L = 183$ mm and 3 mm thickness (mass density 7.85 g/cm^3). The first vibration mode is illustrated in Fig. 21, and one observes that such a mode corresponds to a vibration frequency $\nu_1 = 5.77$ Hz. It tends to activate the primary folding of the structure, being contrasted by the elastic stiffness of the opening cables (Fig. 21). The higher order vibration modes of the system under examination are associated to frequencies much greater than ν_1 (it results, e.g., $\nu_2 = 178\ \nu_1$). This is due to the fact such modes activate the deformation of the stiff steel frames supporting the foldable panels, while the first mode activates the deformation and the elastic response of the nylon cables. We illustrate some of the higher order vibration modes in Fig. S13 of Supplementary Materials. The results presented in Fig. 21 were computed through a Mathematica® code that solves Eq. (64), and were validated against the finite element simulation presented in Supplementary Materials.

It is worth observing that the first natural vibration frequency of a single nylon cable pinned at the extremities, which features a mass density of 1.14 g/cm^3, 0.40 mm diameter and 259 mm length, is approximately equal to 50 Hz, under a tensile force of only 0.1 N. We obtained such a result making use of the formula $\nu_c = 1/(2\sqrt{2}L)\ \sqrt{T/\rho}$, that gives the fundamental transverse vibration frequency of a pinned cable with $\sqrt{2}L$ length. Here, T is tensile force in the cable and ρ is the linear mass density of the material (Shabana, 1996).

Wind loading is a fluctuating action that is expected to lead to a resonant-type response when the structure and/or its parts exhibit natural frequencies below 1 Hz (Holmes, 2018). When instead such frequencies are considerably larger than 1 Hz, as in the case of the mock-up of the solar eye analyzed above, one can reasonably model wind loading as a quasi-static ('background') action. In this context, a static approach ruled by the provisions of international standards as, e.g., the Eurocode 1, EN 1991-1-4:2005 (European Committee for Standardisation, 2005) can be convenient. The study of a resonant response can be conducted, when needed, by generalizing available techniques for large span roofs to building façades equipped with solar eyes (Su et al., 2018). The analysis of such effects, as well those deriving from cross-wind loading, cladding loads and the aerodynamic response of the solar panels attached to the solar eye (Wittwer et al., 2022) is beyond the scope of the present work, and is addressed to future research.

8. Concluding remarks

We have presented the design, modeling and prototyping of novel solar modules with tensegrity architecture that can be employed to tessellate positive-energy solar façades and rooftops with various textures and architectures (Fig. 2). These solar eyes can assume an arbitrary polygonal shape (Fig. 1), and can be integrated into the building façade/rooftop (or parts of these building elements) to form PV cladding systems, solar glazing and windows, and/or adaptive sunscreens, to cite but a few examples Vassiliades et al. (2022), Jayathissa et al. (2017), Alotaibi (2015), Freitas and Brito (2019). The origami-type shape-morphing mechanisms make it possible to operate them by simply adjusting the rest-lengths of the actuation cables, through low energy-consumption electric winches, or also manually, using crank winches. The introduction of the secondary folding motion, the actuation strategy of the primary and secondary folding motions through the simple change of the rest lengths of the cables, and the arbitrary polygonal shape of the unit cell markedly distinguish the current solar module from the origami modules studied in Fraternali et al. (2015b), Babilio et al. (2019), Miranda et al. (2020).

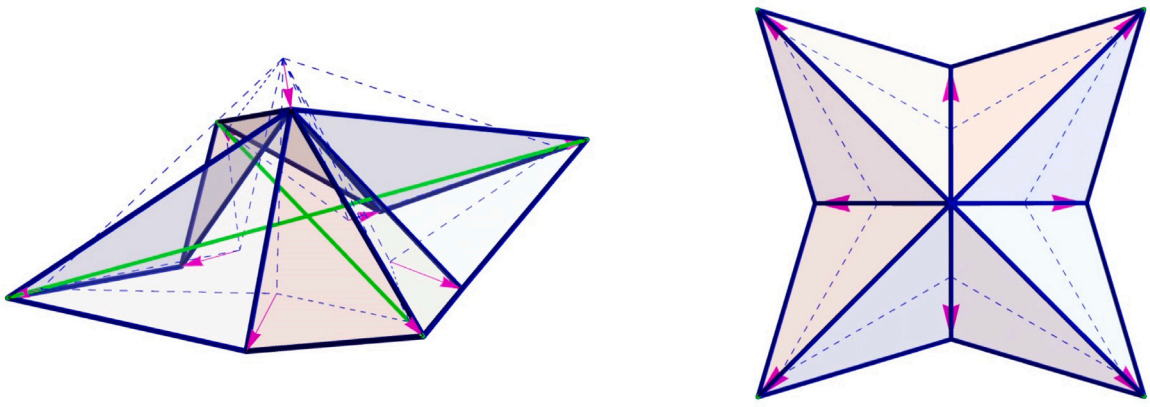

Fig. 21. First vibration mode of the system in Fig. 20 equipped with the dimensions and mechanical properties of the solar eye mock-up (left: 3D view; right: top view; the dashed lines indicate the reference configuration; the node displacements have been graphically amplified for illustration purposes).

We have shown that it is possible to stabilize the primary and secondary folding motions of the analyzed systems by locking the rest lengths of the actuation cables, thus providing suitable stiffness properties against external loads (say, e.g., wind forces). We have also studied the dynamic response of a quadrilateral module through modal analysis, and we have outlined the available procedures to predict the effects of wind loading on such a system. The origami solar eyes can be protected against extreme loading conditions using additional restraining tools, whose design and modeling is left to future work. We also address detailed studies on the mechanical response of the analyzed structures under seismic and/or wind loading, examining experimental loading conditions and conditions drawn from historical records, to future research. The aim will be to detect the effective dynamic properties of such systems and their adaptation to variable loads and displacement capacities. The models developed in this work will be further generalized to account for vibration properties, the balance between import and export energies, as well as deployment- and/or sun tracking-algorithms in a large displacement regime, as a means of designing optimized operation strategies.

Funding

This work was supported by Italian Ministry of University and Research within the PRIN projects with grant numbers 2022P5R22A, P2022PE8BT and 20224LBXMZ (PIs A.A. and F.F.). A.A. also acknowledges support by the Italian Ministry of Foreign Affairs and International Cooperation within the Italy-USA Science and Technology Cooperation Program 2023-2025, Project "Next-generation green structures for natural disaster-proof buildings", grant number US23GR15.

CRediT authorship contribution statement

Fernando Fraternali: Conceptualization, Formal analysis, Funding acquisition, Investigation, Methodology, Project administration, Supervision, Validation, Writing – original draft, Writing – review & editing. **Julia de Castro Motta:** Conceptualization, Data curation, Formal analysis, Investigation, Methodology, Software, Validation, Writing – review & editing. **Giovanni Germano:** Data curation, Investigation, Methodology, Validation, Writing – review & editing. **Enrico Babilio:** Conceptualization, Data curation, Formal analysis, Investigation, Methodology, Validation, Writing – review & editing. **Ada Amendola:** Conceptualization, Formal analysis, Funding acquisition, Investigation, Methodology, Project administration, Supervision, Writing – original draft, Writing – review & editing.

Declaration of competing interest

The authors declare that they have no known competing financial interests or personal relationships that could have appeared to influence the work reported in this paper.

Data availability

Data will be made available on request.

Appendix A. Supplementary data

Supplementary material related to this article can be found online at https://doi.org/10.1016/j.apples.2023.100174.

References

Ala-Juusela, M., Rehman, H.U., Hukkalainen, M., Reda, F., 2021. Positive energy building definition with the framework, elements and challenges of the concept. Energies 14, 6260. http://dx.doi.org/10.3390/en14196260.

Alotaibi, F., 2015. The role of kinetic envelopes to improve energy performance in buildings. J. Archit. Eng. Technol. 04, 149. http://dx.doi.org/10.4172/2168-9717.1000149.

Andreozzi, S., Bessone, G.I., Poala, M.B., Bovo, M., Amador, S.F.D.A., Giargia, E., Niccolai, A., Papetti, V., Mariani, S., 2016. Self-adaptive multi-purpose modular origami structure. Procedia Eng. 161, 1423–1427. http://dx.doi.org/10.1016/j.proeng.2016.08.604.

Armstrong, A., Buffoni, G., Eames, D., James, R., Lyle, L.L.J., Xuereb, K., 2013. The Al Bahar towers: multidisciplinary design for middle east high-rise. Arup J. 60–73.

Attoye, D.E., Aoul, K.A.T., Hassan, A., 2017. A review on building integrated photovoltaic façade customization potentials. Sustainability 9, 2287. http://dx.doi.org/10.3390/su9122287.

Awadh, O., 2017. Sustainability and green building rating systems: LEED, BREEAM, gsas and estidama critical analysis. J. Build. Eng. 11, 25–29. http://dx.doi.org/10.1016/j.jobe.2017.03.010.

Babilio, E., Miranda, R., Fraternali, F., 2019. On the kinematics and actuation of dynamic sunscreens with tensegrity architecture. Front. Mater. 6, 7. http://dx.doi.org/10.3389/fmats.2019.00007.

Bakhshoodeh, R., Ocampo, C., Oldham, C., 2022. Thermal performance of green façades: Review and analysis of published data. Renew. Sustain. Energy Rev. 155, 111744. http://dx.doi.org/10.1016/j.rser.2021.111744.

Bathe, K.-J., Wilson, E.L., 1973. Solution methods for eigenvalue problems in structural mechanics. Internat. J. Numer. Methods Engrg. 6 (2), 213–226. http://dx.doi.org/10.1002/nme.1620060207.

Budiansky, B., 1974. Theory of buckling and post-buckling behavior of elastic structures. Adv. Appl. Mech. 14, 1–65. http://dx.doi.org/10.1016/S0065-2156(08)70030-9.

Çiner, F., Dogan-Saglamtimur, N., 2019. Environmental and sustainable aspects of green building: A review. IOP Conf. Ser.: Mater. Sci. Eng. 706 (1), 012001. http://dx.doi.org/10.1088/1757-899X/706/1/012001.

Chen, T., Bilal, O.R., Lang, R., Daraio, C., Shea, K., 2019. Autonomous deployment of a solar panel using elastic origami and distributed shape-memory-polymer actuators. Phys. Rev. A 11, 064069. http://dx.doi.org/10.1103/PhysRevApplied.11.064069.

Chen, L., Chan, A.P., Owusu, E.K., Darko, A., Gao, X., 2022. Critical success factors for green building promotion: A systematic review and meta-analysis. Build. Environ. 207, 108452. http://dx.doi.org/10.1016/j.buildenv.2021.108452.

De Oliveira, M.C., Skelton, R.E., 2009. Tensegrity Systems. Springer, http://dx.doi.org/10.1007/978-0-387-74242-7.

Elghazi, Y., Wagdy, A., Mohamed, S., Hassan, A., 2014. Daylighting driven design: Optimizing kaleidocycle facade for hot arid climate. In: Fifth German-Austrian IBPSA Conference RWTH Aachen University. pp. 314–321.

European Committee for Standardisation, 2005. EN 1991-1-4: Eurocode 1: Actions on structures, parts 1-4: General actions. Wind actions. Authority: The European Union Per Regulation 305/2011, Directive 98/34/2011, Directive 98/34/EC, Directive 2004/ 18/EC.

Fonseca, L.M., Rodrigues, G.V., Savi, M.A., 2022. An overview of the mechanical description of origami-inspired systems and structures. Int. J. Mech. Sci. 223, 107316. http://dx.doi.org/10.1016/j.ijmecsci.2022.107316.

Fraternali, F., Carpentieri, G., Amendola, A., 2015a. On the mechanical modeling of the extreme softening/stiffening response of axially loaded tensegrity prisms. J. Mech. Phys. Solids 74, 136–157. http://dx.doi.org/10.1016/j.jmps.2014.10.010.

Fraternali, F., Chiara, E.D., Skelton, R.E., 2015b. On the use of tensegrity structures for kinetic solar facades of smart buildings. Smart Mater. Struct. 24, 105032. http://dx.doi.org/10.1088/0964-1726/24/10/105032.

Freitas, S., Brito, M.C., 2019. Solar façades for future cities. Renew. Energy Focus 31, 73–79. http://dx.doi.org/10.1016/j.ref.2019.09.002.

Goodman, R.S., Meier, L.C., 2013. Wind-resistant retractable awning. (U.S Patent 2013/0213587 A1).

Holmes, J.D., 2018. Wind Loading of Structures: Third Edition. pp. 1–682. http://dx.doi.org/10.1201/b18029.

Jayathissa, P., Luzzatto, M., Schmidli, J., Hofer, J., Nagy, Z., Schlueter, A., 2017. Optimising building net energy demand with dynamic BIPV shading. Appl. Energy 202, 726–735. http://dx.doi.org/10.1016/j.apenergy.2017.05.083.

Karanouh, A., Kerber, E., 2015. Innovations in dynamic architecture. J. Facade Des. Eng. 3, 60–73. http://dx.doi.org/10.3233/fde-150040.

Karnan, H., Goyal, R., Majji, M., Skelton, R.E., Singla, P., 2017. Visual feedback control of tensegrity robotic systems. In: IEEE/RSJ International Conference on Intelligent Robots and Systems (IROS). 2017-September, http://dx.doi.org/10.1109/IROS.2017.8206022.

Li, R., Cui, G., 2021. Thermal performance and parametric analysis of a dual-function active solar thermal façade system. J. Build. Eng. 42, 103042. http://dx.doi.org/10.1016/j.jobe.2021.103042.

Li, Y., Pellegrino, S., 2020. A theory for the design of multi-stable morphing structures. J. Mech. Phys. Solids 136, 103772. http://dx.doi.org/10.1016/j.jmps.2019.103772.

Liu, Z., Fang, H., Xu, J., Wang, K., 2023. Digitized design and mechanical property reprogrammability of multistable origami metamaterials. J. Mech. Phys. Solids 173, 105237. http://dx.doi.org/10.1016/j.jmps.2023.105237.

Lu, L., Dai, J., Leanza, S., Hutchinson, J.W., Zhao, R.R., 2023a. Multiple equilibrium states of a curved-sided hexagram: Part II—Transitions between states. J. Mech. Phys. Solids 180, 105407. http://dx.doi.org/10.1016/j.jmps.2023.105407.

Lu, L., Leanza, S., Dai, J., Sun, X., Zhao, R.R., 2023b. Easy snap-folding of hexagonal ring origami by geometric modifications. J. Mech. Phys. Solids 171, 105142. http://dx.doi.org/10.1016/j.jmps.2022.105142.

Mir, M.A., 2011. Green facades and building structures.

Miranda, R., Babilio, E., Singh, N., Santos, F., Fraternali, F., 2020. Mechanics of smart origami sunscreens with energy harvesting ability. Mech. Res. Commun. 105, http://dx.doi.org/10.1016/j.mechrescom.2020.103503.

Miura, K., 1985. Method of packaging and deployment of large membranes in space. The Institute of Space and Astronautical Science report, 618, pp. 1–9.

Miura, K., Pellegrino, S., 2020. Forms and Concepts for Lightweight Structures. Cambridge University Press, http://dx.doi.org/10.1017/9781139048569.

Pesenti, M., Masera, G., Fiorito, F., Sauchelli, M., 2015. Kinetic solar skin: A responsive folding technique. Energy Procedia 70, 661–672. http://dx.doi.org/10.1016/j.egypro.2015.02.174.

Pratapa, P.P., Suryanarayana, P., Paulino, G.H., 2018. Bloch wave framework for structures with nonlocal interactions: Application to the design of origami acoustic metamaterials. J. Mech. Phys. Solids 118, 115–132. http://dx.doi.org/10.1016/j.jmps.2018.05.012.

Salazar, R., Murthy, S., Pellazar, C., Stoica, A., 2017. TransFormers for lunar extreme environments: Large origami deployable solar reflectors. In: 2017 IEEE Aerospace Conference. pp. 1–7. http://dx.doi.org/10.1109/AERO.2017.7943717.

Schenk, M., Guest, S.D., 2013. Geometry of miura-folded metamaterials. Proc. Natl. Acad. Sci. USA 110, 3276–3281. http://dx.doi.org/10.1073/pnas.1217998110.

Seffen, K.A., 2012. Compliant shell mechanisms. Phil. Trans. R. Soc. A 370.1965, 2010–2026. http://dx.doi.org/10.1098/rsta.2011.0347.

Shabana, A.A., 1996. Continuous systems. In: Theory of Vibration: An Introduction. Springer New York, New York, NY, pp. 301–336. http://dx.doi.org/10.1007/978-1-4612-3976-5_7.

Su, N., Peng, S., Hong, N., 2018. Analyzing the background and resonant effects of wind-induced responses on large-span roofs. J. Wind Eng. Ind. Aerodyn. 183, 114–126. http://dx.doi.org/10.1016/j.jweia.2018.10.021.

Sumner, R.W., Popovic, J., 2004. Deformation transfer for triangle meshes. ACM Trans. Graph. 23, 399–405. http://dx.doi.org/10.1145/1015706.1015736.

Tibert, A.G., Pellegrino, S., 2003. Deployable tensegrity masts. In: 44th AIAA/ ASME/ ASCE/AHS/ASC Structures, Structural Dynamics, and Materials Conference. p. 1978. http://dx.doi.org/10.2514/6.2003-1978.

Vassiliades, C., Agathokleous, R., Barone, G., Forzano, C., Giuzio, G.F., Palombo, A., Buonomano, A., Kalogirou, S., 2022. Building integration of active solar energy systems: A review of geometrical and architectural characteristics. Renew. Sustain. Energy Rev. 164, 112482. http://dx.doi.org/10.1016/j.rser.2022.112482.

Wagdy, A., Elghazi, Y., Abdalwahab, S., Hassan, A., 2015. The balance between daylighting and thermal performance based on exploiting the kaleidocycle typology in hot arid climate of Aswan, Egypt. In: AEI 2015: Birth and Life of the Integrated Building - Proceedings of the AEI Conference 2015. pp. 300–315. http://dx.doi.org/10.1061/9780784479070.028.

Wittwer, A.R., Podestá, J.M., Castro, H.G., Mroginski, J.L., Marighetti, J.O., De Bortoli, M.E., Paz, R.R., Mateo, F., 2022. Wind loading and its effects on photovoltaic modules: An experimental–computational study to assess the stress on structures. Sol. Energy 240, 315–328. http://dx.doi.org/10.1016/j.solener.2022.04.061.

Zhai, Z., Wang, Y., Jiang, H., 2018. Origami-inspired, on-demand deployable and collapsible mechanical metamaterials with tunable stiffness. Proc. Natl. Acad. Sci. USA 115, 2032–2037. http://dx.doi.org/10.1073/pnas.1720171115.